*J. Fluid Mech.* (2023), *vol*. 966, A27, doi:10.1017/jfm.2023.457

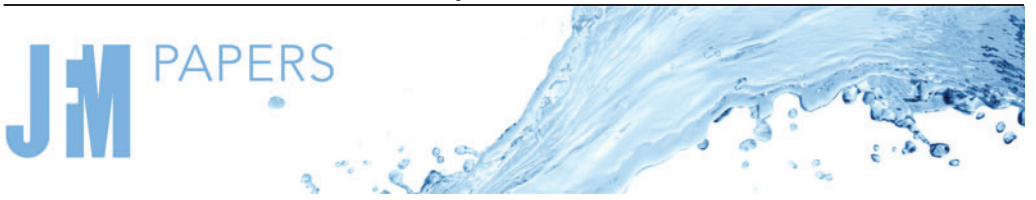


# Liquid entrainment of the toroidal bubble crossing the interface between two immiscible liquids

**Eunseong Moon**[1], **Minho Song**[1] **and Daegyoum Kim**[1],†

[1]Department of Mechanical Engineering, KAIST, Daejeon 34141, Republic of Korea

(Received 21 September 2022; revised 28 March 2023; accepted 19 May 2023)

We experimentally investigate the transport of liquid by a toroidal bubble that rises vertically and penetrates a horizontal interface between two immiscible liquids. Experiments are conducted with various strengths of vortex circulation in the bubble, and with different liquid densities and viscosities. In contrast to a spherical bubble, a rising toroidal bubble carries a great amount of the lower liquid by virtue of the self-induction of circulating flow. The lower liquid is entrained by the toroidal bubble and forms an ellipsoidal body enclosing the bubble after it penetrates the interface. The downward net force acting on the ellipsoidal body results in the radial contraction of the bubble, reducing the volume of the entrained lower liquid. As the entrained volume decreases, the nearby upper liquid eventually pierces the ellipsoidal body, making the bubble unstable. At this instant, the net force acting on the ellipsoidal body approaches zero, and the volume ratio of the entrained lower liquid and bubble converges to a specific value. For smaller vortex circulation and larger density difference between the liquids, the volume of the entrained lower liquid within the ellipsoidal body becomes smaller and the travel distance of the bubble from the initial interface until it becomes unstable decreases. The effective Froude number, which accounts for both the inertial effect of vortex circulation and the gravitational effect of liquid density difference, is found to characterise the temporal changes in the ring radius, propagation speed and entrained volume.

**Key words:** bubble dynamics

† Email address for correspondence: daegyoum@kaist.ac.kr

## 1. Introduction

When a bubble rises under the buoyancy force and passes through a horizontal interface between two immiscible liquids of different densities, some of the lower liquid is transported upwards with the rising bubble in the form of a column (Greene, Chen & Conlin 1991; Magnaudet & Mercier 2020). This liquid column then breaks up into tiny droplets due to the Plateau–Rayleigh instability (Natsui *et al.* 2018). The formation of the liquid column and the droplets dramatically increases the interfacial area between the two liquids. These fluid transport and break-up phenomena can enhance the reaction efficiency in industrial applications by enlarging the interfacial area (Mazumdar & Guthrie 1995). For this reason, fluid entrainment by buoyancy-driven rising bubbles has been used in diverse industrial fields, including metallurgical processes (Greene *et al.* 1991; Reiter & Schwerdtfeger 1992; Natsui *et al.* 2018), solvent extractions (Dietrich *et al.* 2008; Singh, Gebauer & Bart 2017) and air flotation for water treatment (Ghorbanpour-Arani, Rahimian & Haghani-Hassan-Abadi 2020).

Previous studies on the interaction of a bubble with an interface between two immiscible liquids have mostly focused on the use of relatively small spherical and ellipsoidal bubbles (e.g. Dietrich *et al.* 2008; Singh *et al.* 2017; Emery, Raghupathi & Kandlikar 2018; Natsui *et al.* 2018; Mao *et al.* 2020), although Bonhomme *et al.* (2012) considered bubble volumes in the range of approximately 0.01–4 $\mathrm{cm}^3$ and diverse bubble shapes including a toroidal form. Since Walters & Davidson (1963) generated a bubble of toroidal form by injecting a single pulse of air through a narrow tube into a water tank, subsequent studies have confirmed that this can be modelled as a vortex ring under the influence of buoyancy: toroidal bubble (vortex ring bubble) (Pedley 1968; Vasel-Be-Hagh, Carriveau & Ting 2015*a*; Wang *et al.* 2005; Chang & Llewellyn Smith 2018). Compared with spherical bubbles, toroidal bubbles induce a flow in the surrounding fluid, which contributes to self-propagation in addition to the buoyancy force, and possess a relatively large frontal area per unit volume. In addition, Lundgren & Mansour (1991) found that the buoyancy and Kutta–Joukowski lift forces acting on the core of the vortex ring cause the expansion of the ring throughout its propagation. This expansion increases the volume of the fluid flow induced by the ring, namely the entrained fluid volume (Turner 1957; McKim, Jeevanjee & Lecoanet 2020).

Because of the aforementioned salient properties, a toroidal bubble crossing an interface can transport a significant amount of the lower liquid above the interface and remain encapsulated by the lower liquid for a long distance after passing through the interface (Bonhomme *et al.* 2012). In fact, the effectiveness of fluid transport using the entrainment mechanism of a vortex ring has been reported for a single-phase vortex ring composed of the same fluid as the surrounding fluid (Maxworthy 1972; Dabiri & Gharib 2004; McKim *et al.* 2020). However, the toroidal bubble differs from the single-phase vortex ring with regards to the important action of buoyancy. For toroidal bubbles, the effects of buoyancy and the interface between immiscible liquids on fluid transport remain elusive.

By virtue of their buoyant nature and superior fluid transport capabilities, toroidal bubbles represent a promising solution for enhancing the performance of fluid transport and mixing between two immiscible liquid regions in engineering systems. Despite these expected advantages of toroidal bubbles, the work of Bonhomme *et al.* (2012) is the only study, to the best of our knowledge, that has considered the interaction between a rising toroidal bubble and an immiscible liquid interface, primarily for the phase when the bubble passes through the initial position of the interface. In the present study, we experimentally investigate a toroidal bubble crossing the interface between two immiscible liquids (water and oil) from the passage phase to the break-up phase to elucidate the fluid

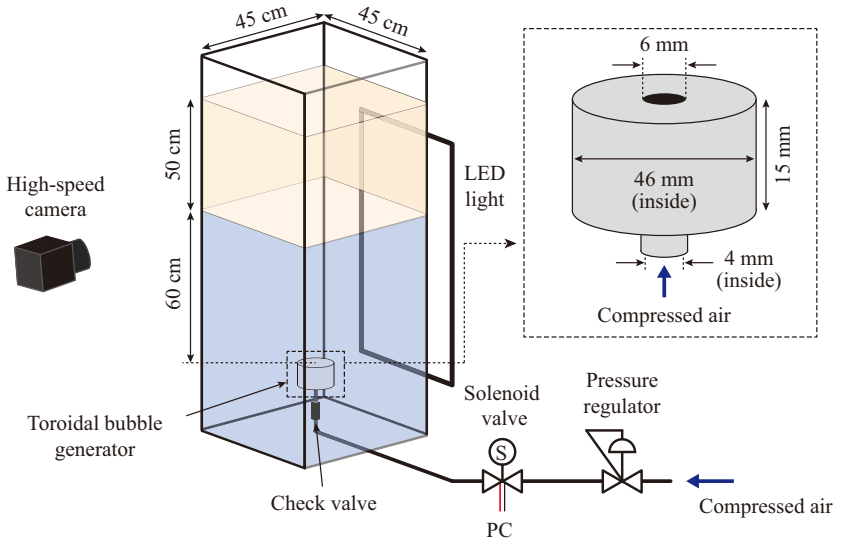


Figure 1. Schematic of the experimental set-up.

transport characteristics. By varying the size and propagation speed of a toroidal bubble, and the fluid properties such as density and viscosity, the key parameters that determine the dynamic behaviour of the toroidal bubble are identified.

The experimental set-up, input parameters and measurement techniques are described in § 2. In § 3, several important quantities relevant to fluid entrainment and transport are analysed. General features of the interactions between the toroidal bubble and the liquid–liquid interface are presented in § 3.1. Then, the ring radius and propagation speed of the bubble, the corresponding liquid volume transported by the bubble and the travel distance of the bubble after it passes through the interface are examined in § 3.2. In § 3.3, the temporal change in the ring radius is predicted through a theoretical approach based on the observations of the previous sections. Furthermore, the effects of the viscosity and density differences between the two liquids are discussed in § 3.4. Finally, our main findings are summarised in § 4.

## 2. Experimental set-up

Experiments were conducted in a glass tank with a square cross-section of 45 cm × 45 cm and a height of 130 cm at 22 ± 1 °C (figure 1). A sufficiently large tank was selected to minimise the blockage effect of sidewalls on the toroidal bubble. A toroidal bubble generator was fabricated, similar to the apparatus of previous studies (Vasel-Be-Hagh *et al.* 2015*b*; Lesage *et al.* 2016; Yan, Carriveau & Ting 2018). This cylindrical apparatus has a small opening on its top (inset of figure 1). Compressed air is supplied from an air compressor to the bubble generator, positioned at the bottom of the water tank, and the air pressure is controlled using a pressure regulator. A solenoid valve in the path of the air is computer-controlled with MATLAB (Mathworks, Inc.). Once the solenoid valve is open for a short duration, the air passes through a check valve which inhibits backflow and then passes into the bubble generator. The air is released through a small opening on the top of the bubble generator. By controlling the air pressure in the range of 25–75 kPa and the valve opening duration in the range of 0.20–0.30 s, toroidal bubbles of various sizes and propagation speeds can be created.

| Upper liquid | Density ($g\,cm^{-3}$) | Kinematic viscosity ($mm^2\,s^{-1}$) | Refractive index |
|---|---|---|---|
| V1 (S-8) | 0.87 | 16.6 | 1.47 |
| V2 (S-8/S-96 mixture) | 0.87 | 80.7 | 1.48 |
| V3 (S-96) | 0.87 | 240.2 | 1.48 |
| **Lower liquid** | **Density** | **Kinematic viscosity** | **Refractive index** |
| | ($g\,cm^{-3}$) | ($mm^2\,s^{-1}$) | |
| Tap water | 1.00 | 0.96 | 1.33 |
| 20 % NaCl solution | 1.15 | 1.31 | 1.37 |

Table 1. Physical properties of the liquids used in experiments at 22 °C.

Two immiscible liquids with different densities were placed in the tank to form a horizontal interface. The lower liquid was filled up to a height of 60 cm above the ejection hole of the bubble generator so that the toroidal bubble had enough space to develop and turn into an axisymmetric shape before impacting the interface. The upper liquid had a height of 50 cm, which is sufficient to observe the evolution of the bubble and interface. To examine the effects of the density difference between the upper and lower liquids, tap water and a 20 % NaCl solution were successively used as the lower liquid. For the upper liquid, three base oils (S-8, S-96, and a mixture of 40.8 % S-8 and 59.2 % S-96, S-Oil, Inc.) were used to investigate variations in the viscosity ratio. For simplicity, base oil S-8, S-8/S-96 mixture and base oil S-96 are hereafter termed to as V1, V2 and V3, respectively, with an increasing order of viscosity. The kinematic viscosity was measured using Zahn cups. The interfacial tension coefficient $\sigma_I$ between the upper and lower liquids was determined using the pendant-drop method (de Gennes, Brochard-Wyart & Quéré 2004), and was found to be in the range of 38–40 $mN\,m^{-1}$. The density, kinematic viscosity and refractive index of the liquids are summarised in table 1.

A high-speed camera (FASTCAM MINI-UX50, Photron Inc.) with a resolution of $1280 \times 1024$ pixels and an AF Nikkor 35 mm f/2D lens (Nikon Corp.) were used to visualise the evolution of the toroidal bubble and the interface between the two liquids. In this condition, one pixel corresponds to 0.72 mm, which is at maximum 3 % of the ring radius. To reduce additional uncertainty from refraction through liquids and the wall of the tank, the camera was located at a sufficient distance of 240 cm from the water tank and facing the centre of the interface horizontally. The images were captured at 125 frames per second with an exposure time ranging from 0.16 ms to 0.40 ms. The image plane was illuminated using a light-emitting diode plate light located on the opposite side of the tank to enhance the contrast of images; see figure 1.

To obtain velocity fields around a toroidal bubble in the lower fluid, particle image velocimetry (PIV) was performed. Polyamide particles (Vestosint 1164 white, Evonik Industries AG.) with a density of $1.06\,g\,cm^{-3}$ and a mean diameter of 50 μm were used as seeding particles. A planar laser sheet was generated vertically by a 10 W continuous laser (MGL-W-532A, CNI Co.), and it included the path of the rising toroidal bubble centre on the $xz$-plane in figure 2(*b*). For PIV, the same high-speed camera was used to capture the images at 1000 frames per second, and the exposure time was in the range of 0.8–1.0 ms. The multi-grid cross-correlation method (PIVview2C 3.6.0, PIVTEC GmbH) was used to process image pairs; the time interval between two images in a pair was 1 ms. The initial and final window sizes were $32 \times 32$ pixels and $16 \times 16$ pixels, respectively, with an overlap of 50 %, which created $79 \times 55$ nodes with a spatial resolution of 5.1 mm.

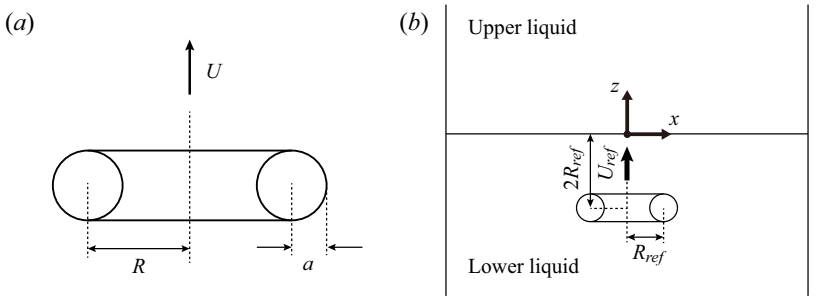


Figure 2. (*a*) Parameters of the toroidal bubble and (*b*) its ring radius $R_{ref}$ and propagation speed $U_{ref}$ at the reference time $t = t_{ref}$. At this instant, the centre point of the toroidal bubble is positioned at twice the ring radius below the horizontal interface.

Flow regions which are not accessible by PIV, such as the shadow of the bubble and the region near multiple interfaces with laser light scattered, were obtained by interpolating nearby velocity data. PIV was conducted for a limited number of cases to identify the flow pattern around the toroidal bubble. PIV results for the bubble after penetration were not reliable due to refraction in the entrained lower fluid and surrounding upper fluid, and thus the phase after penetration was not considered for PIV.

The interaction between the approaching toroidal bubble and the interface depends on the shape and propagation speed $U$ of the bubble. The bubble shape is determined by its ring radius $R$ and vortex core radius $a$, under the assumption that the bubble is a circular toroid (figure 2*a*). Note that the $x$- and $z$-axes are in the horizontal and vertical directions, respectively, and $x = 0$ denotes the centre of the bubble, while the initial position of the interface is set to $z = 0$ (figure 2*b*). The interface of a toroidal bubble was challenging to detect automatically from image processing because the interface of the front half of the bubble with respect to its distance from the camera overlapped the interface of the other half of the bubble. Therefore, we measured the ring radius, core radius and position of the bubble manually. The core diameter was measured from a distance between the uppermost and lowermost points of the front half of the bubble (i.e. the part that is closer to the camera), while the ring diameter was measured by subtracting the core diameter from the length between the left and right ends of the bubble. The propagation speed was computed by the central difference scheme using the position data of the ring's centre along the $z$-axis with a time step of 0.16 s, and the bubble volume $V_b$ was estimated as $V_b = 2\pi^2 R a^2$ under the assumption of a perfectly toroidal form. These data were corrected to account for the difference in the refractive indices of the two liquids; see Appendix A.

Because the three parameters ($U$, $R$ and $a$) are time-dependent, their values at either specific instant or position should be chosen as reference values. The reference position was chosen such that the bubble at this position barely changed the interface. We found that the deformation of the interface was negligible when the centre of the bubble was positioned at twice the ring radius below the initial horizontal interface, and thus this position and corresponding instant were regarded as the reference position and reference time $t_{ref}$, respectively. The propagation speed, ring radius and core radius of the bubble at $t = t_{ref}$ were defined as reference values: $U_{ref}$, $R_{ref}$ and $a_{ref}$, respectively (figure 2*b*). The bubble volume at $t = t_{ref}$ was also defined as the reference bubble volume $V_{b,ref}$. The mean absolute percentage errors of $U_{ref}$, $R_{ref}$, $a_{ref}$ and $V_{b,ref}$ due to the spatial resolution of images are 1.0 %, 1.3 %, 7.4 % and 14.3 %, respectively. Here, the relatively large error of $V_{b,ref}$ was due to the accumulated errors from $R_{ref}$ and $a_{ref}$. To reduce the error in

measuring $V_{b,ref}$, the values from five images taken at 0.04 s intervals around the reference position were averaged.

The strength (circulation) of vortical flow around a toroidal bubble has a critical influence on the dynamic behaviours of the bubble. According to Vasel-Be-Hagh *et al.* (2015*a*), the circulation of a toroidal bubble in a single liquid can be estimated analytically as

$$\Gamma = 4\pi RU\left(\ln\frac{8R}{a} - \frac{1}{4}\right)^{-1}. \tag{2.1}$$

A comparison with the PIV results confirmed that the use of (2.1) based on the ring radius, propagation speed and core radius of the toroidal bubble provided a reasonable estimate of its circulation before the bubble crosses the interface; see Appendix B. Throughout this study, therefore, the circulation of the toroidal bubble is obtained from (2.1), and the reference circulation at $t = t_{ref}$ is termed $\Gamma_{ref}$.

For a single-phase vortex ring impinging a density-stratified interface, the relative magnitudes of the inertial force and gravitational force acting on the vortex ring are crucial in characterising the interaction between the vortex ring and the interface (e.g. Linden 1973; Dahm, Scheil & Tryggvason 1989; Stock, Dahm & Tryggvason 2008; Advaith *et al.* 2017; Olsthoorn & Dalziel 2017; Song, Choi & Kim 2021; Wang & Feng 2022). Regarding the penetration of a spherical or ellipsoidal bubble through an interface between two immiscible liquids, the viscosity difference also affects the volume of the fluid entrained by the bubble (Greene *et al.* 1991; Bonhomme *et al.* 2012). The Froude number $Fr$, which represents the relative magnitude of the inertial and gravitational forces for a toroidal bubble, the viscosity ratio $\Lambda$ between the two liquids, and the Atwood number $At$, which is a dimensionless form of the density difference between two liquids, are employed as the main dimensionless variables to take these effects into account:

$$Fr = \frac{\Gamma_{ref}}{(gR_{ref}^3)^{1/2}}, \tag{2.2a}$$

$$\Lambda = \frac{\mu_u}{\mu_l}, \tag{2.2b}$$

$$At = \frac{\rho_l - \rho_u}{\rho_l + \rho_u}, \tag{2.2c}$$

where $\mu$ and $\rho$ are the dynamic viscosity and density, respectively, and subscripts $l$ and $u$ denote the lower and upper liquids, respectively. The reference circulation $\Gamma_{ref}$ of the toroidal bubble replaces the inertial component of the Froude number, similar to the definition given by Song, Bernal & Tryggvason (1992); $R_{ref}$ is the reference ring radius. As the gravitational force of the toroidal bubble is closely related to the density difference across the interface, we will consider a parameter that combines $Fr$ and $At$ to identify the coupled effects of density difference and bubble inertia in § 3.4. The ranges of these dimensionless parameters are $Fr = 0.9$–$2.5$, $At = 0.067$–$0.133$ and $\Lambda = 15.1$–$217.9$. Here, the range of $Fr$ is such that a stable toroidal bubble penetrates the interface; for very small values of $Fr$, bubbles from the generator cannot form a toroid, whereas for very large values of $Fr$, the bubbles become unstable and wrinkled before reaching the interface.

The Bond number ($= \rho_l g D_{eq}^2/\sigma_S$), where $D_{eq} = (6V_{b,ref}/\pi)^{1/3}$ is the equivalent diameter and $\sigma_S$ is the surface tension coefficient for the interface between the air and the lower liquid, and the Archimedes number ($= \rho_l g^{1/2} D_{eq}^{3/2}/\mu_l$) are also known to play a role in the three-phase system involving relatively small bubbles (Bonhomme *et al.* 2012). However, a toroidal bubble can only appear for high Bond and Archimedes numbers

(Bonometti & Magnaudet 2006; Tripathi, Sahu & Govindarajan 2015). Because we aim to identify the behaviours of toroidal bubbles, we only consider sufficiently high Bond and Archimedes numbers (over 100 and 10 000, respectively), and these parameters did not show significant effects on the interactions between the bubble and the interface for the range available in our apparatus.

To compare various cases in which $Fr$, $\Lambda$ or $At$ differs, the ring radius $R$ and propagation speed $U$ are normalised by the reference values $R_{ref}$ and $U_{ref}$, respectively. Also, the dimensionless time $t^*$ is introduced as

$$t^* = \frac{\Gamma_{ref}(t - t_0)}{R_{ref}^2}, \tag{2.3}$$

where $t_0$ is the instant at which the uppermost point of the toroidal bubble passes the original horizontal position of the interface. At the initial stage of toroidal bubble formation, in which the bubble is approximately spherical, a liquid jet from its bottom surface causes a high-speed and intense flow (Chen *et al.* 1999; Bonometti & Magnaudet 2006; Cao & Macián-Juan 2020). The shape and propagation speed of the resultant toroidal bubble were varied although the air pressure and valve opening time were kept unchanged in our experiments. This inconsistency is because the bubble formation process is sensitive even to slight disturbance of the flow. Accurate control and perfect prediction of the initial toroidal bubble configuration were infeasible. Although the dimensional values of the reference ring radius, propagation speed and circulation were different among several trials, very similar dynamic behaviours appeared in a dimensionless sense (i.e. temporal changes in normalised $R/R_{ref}$, $U/U_{ref}$) when $Fr$, $\Lambda$ and $At$ were identical.

## 3. Results and discussion

### 3.1. *Overview of toroidal bubble–interface interactions*

As the behaviours of a toroidal bubble after passing through the liquid–liquid interface remain elusive, we first describe general features regarding the evolutions of the toroidal bubble and interface. The sequential images of the toroidal bubble and interface are displayed in figure 3(*a*), and the corresponding ring radius and propagation speed are shown in figure 3(*b*,*c*). Although one specific case is presented in figure 3(*a*), the behaviours demonstrated in the figure are generally observed in the other cases in which the bubble penetrates the interface. These data were tracked until the lower liquid surrounding the bubble became corrugated due to instability because the corrugated interface made the accurate correction of refraction impossible.

When the toroidal bubble rises far below the horizontal interface ($t^* < -1$ in figure 3), the bubble hardly interacts with the interface, and it gradually expands the ring radius while reducing the propagation speed. This expansion is common for a toroidal bubble rising vertically in a single uniform fluid (Pedley 1968; Cheng, Lou & Lim 2013; Vasel-Be-Hagh *et al.* 2015*a*). As the bubble approaches the interface, the interface starts to deform into an ellipsoidal cap (figure 3*a*, $t^* = -2.8$). Simultaneously, the radial expansion accelerates, and the propagation speed declines drastically (figure 3*b*,*c*, $t^* \approx 0$). These trends of the ring radius and the propagation speed are also observed as a single-phase vortex ring perpendicularly approaches a flat surface or a horizontal density-stratified interface (Walker *et al.* 1987; Olsthoorn & Dalziel 2017; Xu *et al.* 2017; Yeo *et al.* 2020).

As the toroidal bubble crosses the initial position of the interface, it moves upwards along with some of the lower liquid instead of passing the interface alone. The lower liquid forms an ellipsoid that envelops the toroidal bubble, preventing direct contact

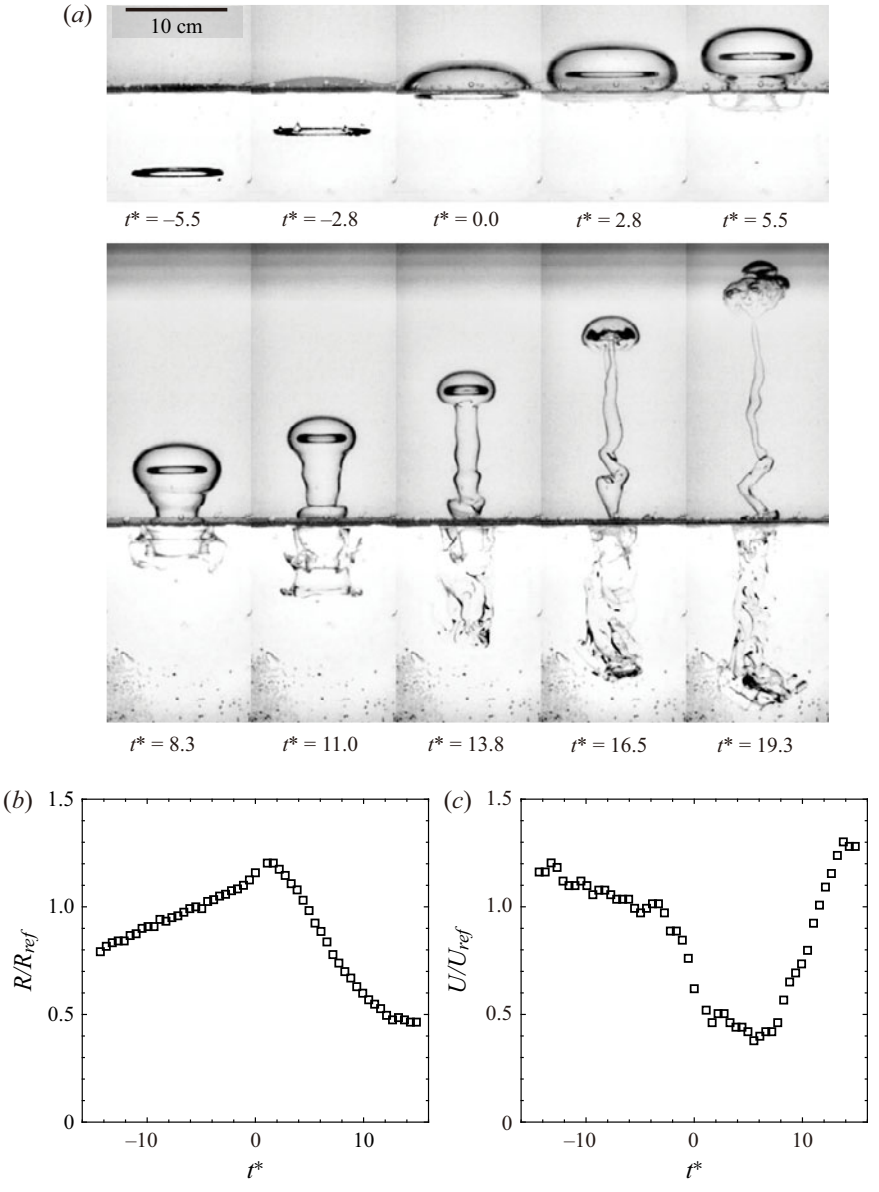


Figure 3. (*a*) Sequential images of the toroidal bubble rising through an interface between two immiscible liquids for $Fr = 0.9$, $\Lambda = 73.2$ and $At = 0.067$. (*b*,*c*) Temporal changes in the normalised ring radius and propagation speed. See supplementary movie 1 available at https://doi.org/10.1017/jfm.2023.457 for panel (*a*).

between the bubble and the upper liquid (figure 3*a*, $t^* = 2.8$). Although the horizontal interface at a decent distance from the bubble is lowered by up to 0.3 cm at this point as the lower liquid moves upwards, the dynamics of the bubble are hardly affected by the change in the interface level. After penetration, the ring radius and the volume of the lower liquid surrounding the bubble begin to decrease. The reduced volume of the surrounding liquid results in the vertical liquid column being formed below the bubble. This falling liquid column creates secondary vortices below the initial location of the interface, which rotate in the direction opposite to the flow around the toroidal bubble

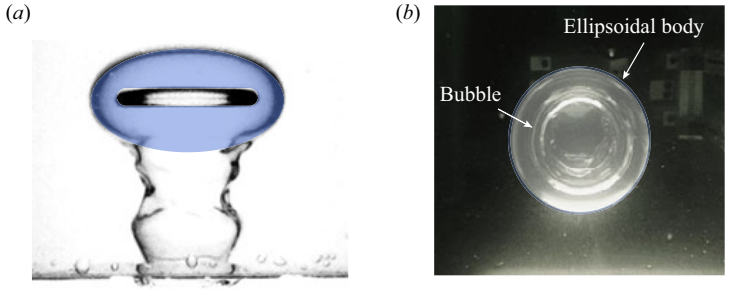


Figure 4. (*a*) Side view of entrained lower liquid. The blue area denotes the entrained lower fluid consisting of an *ellipsoidal body* with a toroidal bubble. (*b*) Top view of entrained lower fluid.

(figure 3*a*, $t^* \geq 5.5$). The radially contracting bubble accelerates and rises with a greater speed (figure 3*b*,*c*, $t^* > 6$). In the later stage, the ring radius and the volume of the lower liquid enveloping the bubble become quite small, with most of the lower liquid lost to the falling liquid column (figure 3*a*, $t^* = 11.0$). The toroidal bubble then becomes unstable, losing its axisymmetric form (figure 3*a*, $t^* = 16.5$); we discuss the origin of this instability in § 3.2. The unstable bubble eventually breaks up into tiny bubbles, primarily in the form of a spherical cap (figure 3*a*, $t^* = 19.3$). The remaining lower liquid near the tiny bubbles loses its momentum and begins to fall down.

The lower liquid encapsulating the toroidal bubble fits into an ellipse when observed from the side, as highlighted in figure 4(*a*), and it is axisymmetric with respect to the longitudinal $z$-axis (figure 4*b*). Therefore, we assume that the three-dimensional shape is ellipsoidal, and the combination of the bubble and the lower liquid encapsulating the bubble is termed an ellipsoidal body hereafter. The lower liquid encapsulating the bubble is a salient feature in the penetration of the toroidal bubble. Although non-toroidal bubbles, such as spherical or spheroidal, also lift some of the lower liquid under the same circumstance, only a thin film of the lower liquid surrounds the bubble, and the rest is mostly below the bubble in the form of a liquid column (Reiter & Schwerdtfeger 1992; Bonhomme *et al.* 2012; Natsui *et al.* 2018).

When the toroidal bubble is below the initial horizontal interface, the vortical flow of the lower liquid is accompanied by the toroidal bubble, as can be seen from the velocity field (in the laboratory reference frame) measured by PIV (figure 5*a*); in the figure, the bubble is positioned at the reference position. The velocity field in the reference frame moving with the centre of the bubble can be acquired by superimposing the propagation speed of the bubble at this instant on the velocity field in the laboratory reference frame (figure 5*b*). In this moving reference frame, the ellipsoidal boundary, which consists of streamlines enclosing the toroidal bubble, is constructed (red dashed line in figure 5*c*). This boundary can be regarded as the boundary of the vortex ring within which the lower liquid is entrained by the vortical flow (Dabiri & Gharib 2004). As the toroidal bubble passes through the liquid–liquid interface, the generated ellipsoidal body depicted in figure 4(*a*) is similar to the ellipsoidal boundary of the flow structure in figure 5(*c*). That is, the entrained volume of the lower liquid inside the ellipsoidal body originates from the vortical flow formed around the toroidal bubble below the horizontal interface. Although reliable velocity fields could not be obtained due to refraction through the interfaces and the data are not presented here, the vortical flow around the toroidal bubble inside the ellipsoidal body is also observed after the bubble penetrates the original interface.

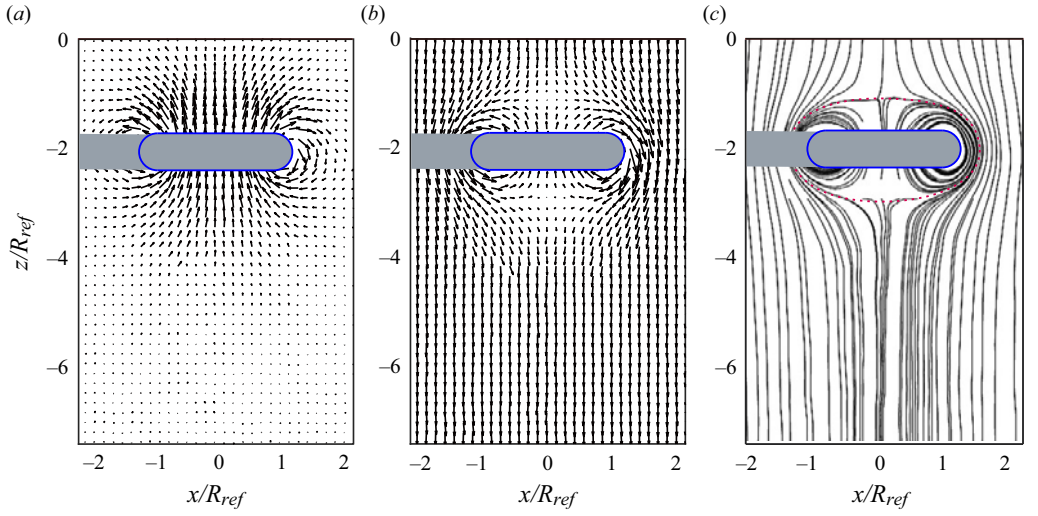


Figure 5. (*a*) Instantaneous velocity field around the toroidal bubble below the initial interface in the laboratory reference frame, (*b*) instantaneous velocity field in the reference frame moving with the toroidal bubble and (*c*) instantaneous streamlines from the velocity field in panel (*b*). The blue solid lines and greyed-out areas in panels (*a–c*) denote the toroidal bubble and the shadow of the bubble, respectively, and the red dashed line in panel (*c*) denotes the boundary of the toroidal bubble in the frame moving with the bubble. Here, $Fr = 2.5$, $\Lambda = 9.7$ and $At = 0.067$.

### 3.2. *Toroidal bubble dynamics and entrained volume*

The passage of a toroidal bubble through the liquid–liquid interface exhibits a common pattern, as reported in § 3.1. However, the behaviours of the toroidal bubble, such as ring radius and propagation speed, and the entrained volume of the lower liquid depend on the conditions of the system. In this section, we examine the effects of the Froude number $Fr$ by varying the circulation of the vortical flow around the bubble. The lower and upper liquids are fixed as tap water and V2 oil, respectively: $\Lambda = 73.2$ and $At = 0.067$.

Temporal changes in the normalised ring radius $R/R_{ref}$ and propagation speed $U/U_{ref}$ are depicted in figure 6 for six values of $Fr$. The corresponding values of $R_{ref}$, $U_{ref}$, $V_{b,ref}$ and $\Gamma_{ref}$ are listed in table 2 for each case of $Fr$. The trends in the ring radius and propagation speed are similar among the six cases, demonstrating that the trends illustrated by figure 3(*b*,*c*) can be generalised. Although $R/R_{ref}$ and $U/U_{ref}$ are hardly affected by $Fr$ before crossing the interface, distinct differences appear after passing the interface. Lower values of $Fr$ produce steeper reductions in $R/R_{ref}$ and $U/U_{ref}$ after $t^* = 0$, followed by steeper growth in $U/U_{ref}$ after approximately $t^* = 6$. This steeper growth in $U/U_{ref}$ appears to begin when the bubble rises sufficiently high to form the liquid column connected with the ellipsoidal body. The relative magnitude of vortex strength is small for lower $Fr$, and the inertial effects of the bubble on the penetration into the upper liquid are accordingly weak, causing a more dramatic reduction in $R/R_{ref}$ and $U/U_{ref}$ as the bubble crosses the interface.

Another main interest is to evaluate how much of the lower liquid the toroidal bubble can entrain and carry upwards across the interface. As shown in figure 5(*c*), the ellipsoidal boundary of the toroidal bubble in the reference frame fixed with the bubble is caused by the circulatory flow near the bubble. Several studies of the vortex ring have defined the entrained volume as the volume of the fluid inside the ellipsoidal boundary (Dabiri & Gharib 2004). Similarly, the ellipsoidal body in the upper fluid is formed by the

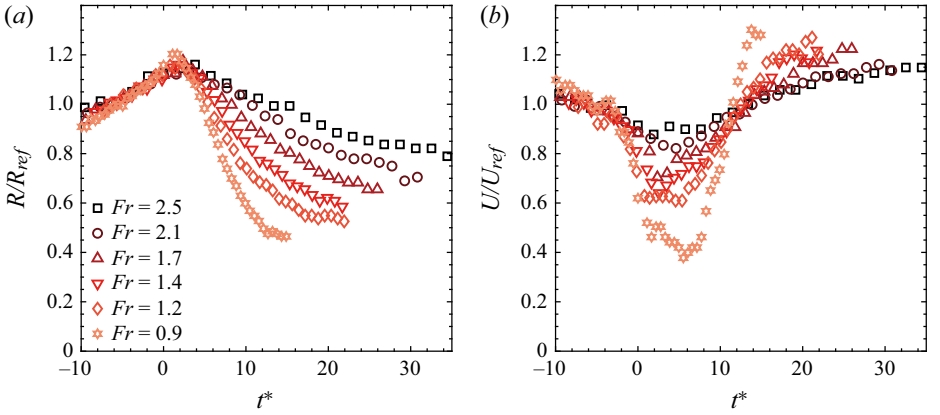


Figure 6. Temporal changes in (*a*) normalised ring radius $R/R_{ref}$ and (*b*) propagation speed $U/U_{ref}$ for $Fr = 0.9$–$2.5$ ($\Lambda = 73.2$ and $At = 0.067$). In each case, data are presented while the bubble remains stable, and a smooth bubble interface can be clearly observed.

| $Fr$ | $\Lambda$ | $At$ | $R_{ref}$ (cm) | $U_{ref}$ (cm s$^{-1}$) | $V_{b,ref}$ (cm$^3$) | $\Gamma_{ref}$ (cm$^2$ s$^{-1}$) |
|---|---|---|---|---|---|---|
| 2.5 | 73.2 | 0.067 | 2.77 | 37.5 | 12.5 | 366.8 |
| 2.1 | 73.2 | 0.067 | 2.98 | 33.8 | 13.0 | 341.9 |
| 1.7 | 73.2 | 0.067 | 3.26 | 29.6 | 12.7 | 313.5 |
| 1.4 | 73.2 | 0.067 | 3.81 | 27.9 | 13.0 | 330.1 |
| 1.2 | 73.2 | 0.067 | 3.94 | 25.7 | 12.5 | 305.6 |
| 0.9 | 73.2 | 0.067 | 4.29 | 20.7 | 10.2 | 254.1 |

Table 2. Reference values of the toroidal bubble for each case of $Fr$ with $\Lambda = 73.2$ and $At = 0.067$.

circulatory flow near the toroidal bubble. In this sense, the volume inside the ellipsoidal body, excluding the liquid column volume, is only considered for the entrained volume. Consequently, the volume of the ellipsoidal body subtracted by the bubble volume is defined as the entrained volume, $V_e$, in this study.

In our experiments, toroidal bubbles rose stably to approximately 30 cm above the reference position. The hydrostatic pressure, which considers the densities of the upper and lower liquids, changes along the vertical direction from the reference position. With the adiabatic assumption, the volume change over this vertical distance by the hydrostatic pressure difference is estimated to be approximately 2 %. As the bubble volume is much smaller than the entrained volume, this 2 % change in the bubble volume is negligible in estimating the entrained volume. Thus, the bubble volume is assumed to be constant throughout its penetration phase: $V_b = V_{b,ref}$. The entrained volume is measured from the instant at which the lowermost part of the bubble passes through the initial position of the interface until the bubble and the enveloping lower liquid become unstable and asymmetric. When the entrained volume is not in a completely ellipsoidal form and the liquid column has not yet formed (see figure 3*a*, $t^* = 2.8$), only the volume above the initial position of the interface is considered.

The temporal variations in the entrained volume $V_e$, made dimensionless by $R_{ref}^3$, are depicted in figure 7(*a*) for six values of $Fr$ (in table 2). The entrained volume drops quickly after the bubble crosses the interface. A greater decrease in $V_e/R_{ref}^3$ is observed for lower

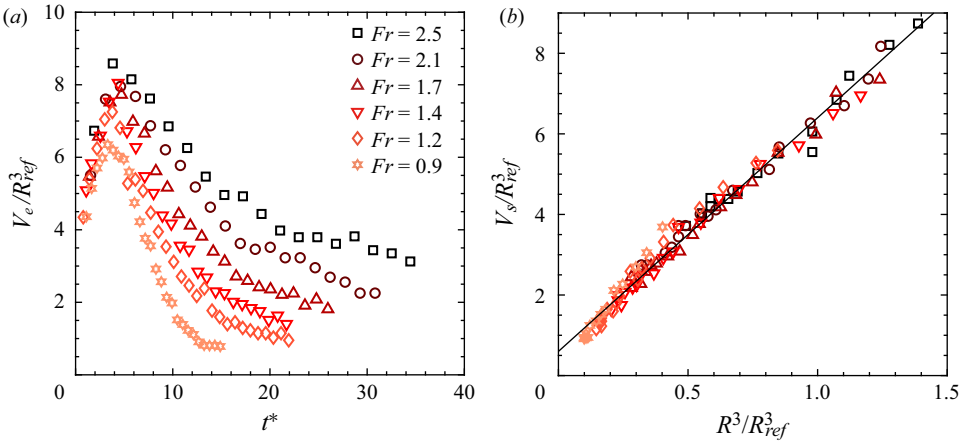


Figure 7. (*a*) Temporal changes in normalised entrained volume $V_e/R_{ref}^3$ and (*b*) normalised volume of the ellipsoidal body, $V_s/R_{ref}^3$, versus normalised ring radius cubed, $(R/R_{ref})^3$, for $Fr = 0.9$–$2.5$ ($\Lambda = 73.2$ and $At = 0.067$). The black solid line is from (3.1).

values of $Fr$. Comparing figures 6(*a*) and 7(*a*), the tendency of the entrained volume is quite similar to that of the ring radius $R$, suggesting the possibility of predicting the entrained volume based on the ring radius.

The correlation between the ring radius and entrained volume of the toroidal bubble becomes apparent when the bubble is sufficiently far above the initial position of the interface (i.e. $z \geq R_{ref}$) to allow the lower liquid encapsulating the bubble to become almost ellipsoidal. The normalised volume of the ellipsoidal body, $V_s/R_{ref}^3$, is plotted versus $(R/R_{ref})^3$ for the six values of $Fr$ ($\Lambda = 73.2$ and $At = 0.067$) in figure 7(*b*). Regardless of $Fr$, these parameters collectively exhibit a linear relationship with a non-zero $y$-intercept. As $R$ approaches zero, the bubble becomes spherical, having the non-zero volume of the ellipsoidal body. Thus, a non-zero $y$-intercept is reasonable. Using the least-squares method, the following empirical relation with an R-squared value of 0.97 is acquired:

$$V_s = V_e + V_{b,ref} = 5.8R^3 + 0.6R_{ref}^3. \tag{3.1}$$

Even for other values of $\Lambda$ and $At$ considered in this study, the data for $V_s/R_{ref}^3$ and $(R/R_{ref})^3$ fit well into (3.1), suggesting the universal similarity of the ellipsoidal body with respect to the ring radius.

This similarity suggests that the ellipsoidal boundary of the toroidal bubble in the reference frame fixed with the bubble (red dashed line in figure 5*c*) before penetration retains its shape throughout the penetration process. For general vortex rings in a single phase, the shape of the ellipsoidal boundary is dependent on the flow structure of the vortex ring (Norbury 1973). However, in the present study, due to the unavailability of velocity fields after penetration, it is difficult to reliably analyse the flow structure near the bubble after penetration. Hence, the explanation of the correlation between $V_s/R_{ref}^3$ and $(R/R_{ref})^3$ is limited to be conjectural, based on the observation that the boundary shape of the toroidal bubble before penetration is similar to the boundary shape of the ellipsoidal body after penetration (figures 4*a* and 5*c*).

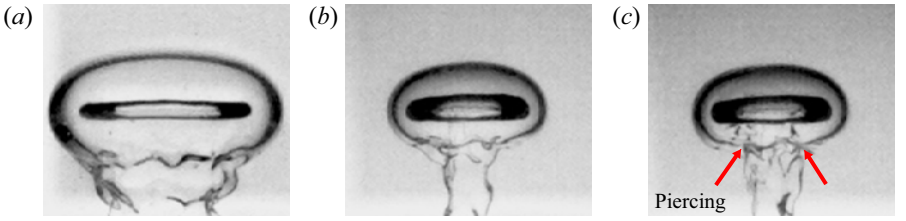


Figure 8. Piercing process of the upper liquid into the lower liquid encapsulating the toroidal bubble. See supplementary movie 2.

How long the ellipsoidal body rises stably is also examined in a qualitative manner. When the toroidal bubble shrinks and the entrained volume decreases (figure 7), the lower liquid falling from the ellipsoidal body forms a thick liquid column (figure 8*a*). Up to this stage, the liquid falling through the column obstructs the piercing of the upper liquid into the ellipsoidal body on the lower side of the ellipsoidal body. As the bubble travels farther, the reduction in the entrained volume becomes slower, and the flux of the lower liquid falling through the column decreases, resulting in a thinner column (figure 8*b*). The slender column becomes corrugated due to instability, just as in the case of a single-phase vortex ring crossing a density-stratified interface (Advaith *et al.* 2017), and the bottom surface of the ellipsoidal body becomes unstable. The upper liquid around the ellipsoidal body then pierces the ellipsoidal body through its bottom interface (figure 8*c*).

The piercing of the upper liquid can occur when the reduction in the ring radius becomes slower, and it commences near the bottom of the ellipsoidal body in all experimental cases, because the circulation of the toroidal bubble induces an inward flow of the entrained liquid near the bottom surface; see figure 5(*a*). Soon after the piercing, the ellipsoidal body becomes asymmetric, accelerating the instability of the bubble. We confirmed that this kind of instability was not observed for a toroidal bubble rising in a single liquid in the range of $Fr$ used in our experiments. In addition, Pedley (1968) theoretically predicted that the height to which a toroidal bubble with a volume of 21 cm$^3$ could rise stably was over 150 cm when it was immersed in a single liquid. In contrast, $h_{stable}$ is mainly below 30 cm in the present study, suggesting that the piercing of the upper liquid is the primary cause of the instability in our cases.

After the piercing, the bubble breaks up at an instant. Although the entrained liquid still has a little momentum, this height at which the piercing occurs appears to be the clear limit of the stable transport height of the toroidal bubble as the bubble breaks shortly. Hence, the height of the bubble centre at which the piercing begins, $h_{stable}$, is regarded as a characteristic travel distance to represent the effectiveness of fluid transport across the interface. This distance is measured from the original position of the interface (figure 9*a*). The travel distance $h_{stable}$ is correlated with the Froude number. For high values of $Fr$, the ellipsoidal body possesses large inertia, which makes it more stable and thus delays the piercing of the upper liquid. Indeed, $h_{stable}/R_{ref}$ tends to increase linearly with $Fr$ (figure 9*b*).

To evaluate how effectively the entrained volume $V_e$ is transported until the centre of the toroidal bubble reaches $z = h_{stable}$ for a given volume of the toroidal bubble, figure 10 plots $V_e$ normalised by the reference bubble volume $V_{b,ref}$ with respect to the vertical position of the bubble centre, $z$, normalised by $h_{stable}$ (see figure 2*b* for the definition of the $z$-coordinate). With decreasing $Fr$, $V_e/V_{b,ref}$ becomes greater around $z/h_{stable} = 0.1$–$0.2$, which seems to conflict with the results shown in figure 7. However, this result is reasonable when the definition of the Froude number (2.2*a*) is considered.

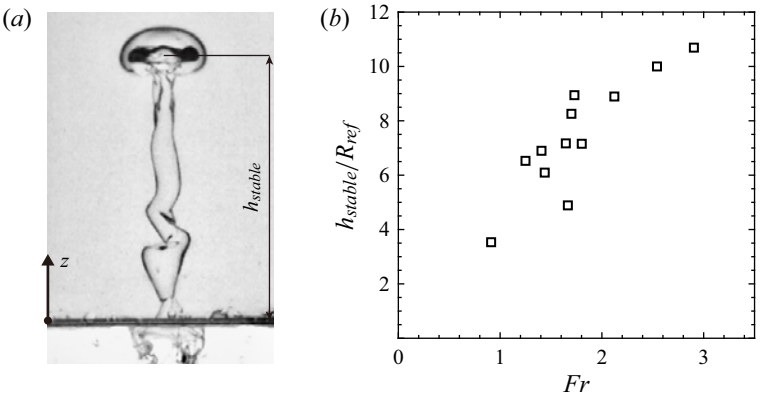


Figure 9. (*a*) Definition of characteristic travel distance $h_{stable}$ and (*b*) travel distance normalised by reference ring radius, $h_{stable}/R_{ref}$, versus $Fr$ ($\Lambda = 73.2$ and $At = 0.067$).

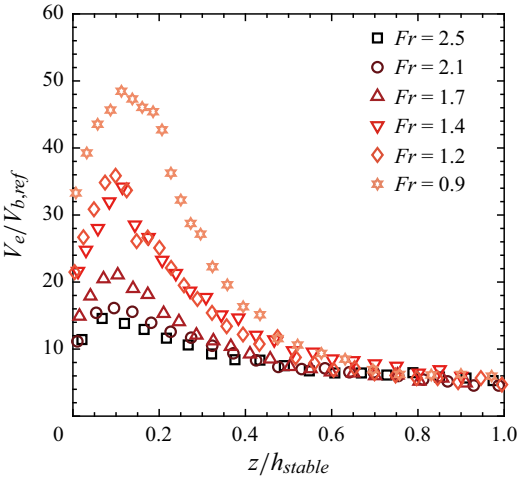


Figure 10. Entrained volume normalised by bubble volume, $V_e/V_{b,ref}$ with respect to dimensionless height $z/h_{stable}$ of the toroidal bubble for $Fr = 0.9$–$2.5$ ($\Lambda = 73.2$ and $At = 0.067$).

In our experiments, lower values of $Fr$ tend to produce bubbles with a greater reference ring radius $R_{ref}$ (see table 2), which leads to a large entrained volume $V_e$ immediately above the initial position of the interface. Remarkably, just after crossing the interface, the bubble carries a massive amount of the lower liquid, approximately 15–50 times its volume $V_{b,ref}$ up to $z/h_{stable} = 0.1$–$0.2$, even without including the volume of the liquid column (figure 10).

It is worth comparing the performance of liquid transport between the toroidal bubble and non-toroidal bubbles. Non-toroidal bubbles rising in a single liquid have various shapes depending on their size and liquid properties such as viscosity and surface tension coefficient, and their paths are also diverse, in addition to vertical straight motion without oscillation, because of instability (Magnaudet & Mougin 2007; Tripathi *et al.* 2015; Sharaf *et al.* 2017). When a non-toroidal bubble passes through a liquid–liquid interface, the colliding angle between the bubble and the interface also plays a big role (Choi & Park 2021). Although the trajectory and colliding angle are regarded as critical parameters for

liquid transport, only a few cases of non-toroidal bubbles are chosen for comparison with the toroidal bubble. To compare the toroidal bubble and non-toroidal bubbles of the same volume, an equivalent diameter $D_{eq} = (6V_{b,ref}/\pi)^{1/3}$ is useful. According to Bonhomme *et al.* (2012), the total volume of the lower liquid transported by a vertically ascending spherical bubble (including the volume of the liquid column below the bubble) is three times the bubble volume when the vertical position of the bubble is around $z = D_{eq}$. The volume of the transported liquid drops quickly afterwards and reaches zero at $z = 4D_{eq}$ (figures 4 and 5 in Bonhomme *et al.* 2012). The volume of the transported lower liquid by a spherical cap bubble rising vertically (including the liquid column) reaches up to seven times the bubble volume at $z = 4D_{eq}$ (figures 8 and 9 in Bonhomme *et al.* 2012). Furthermore, Choi & Park (2021) reported that bubbles in zigzagging paths transported the lower liquid for a distance much shorter than bubbles in rocking motion; bubbles in rocking motion can rise with the lower liquid approximately by $5D_{eq}$ from the position of the undisturbed interface.

By comparison, the maximum entrained volume of the toroidal bubble (excluding the liquid column) is roughly 15–50 times the volume of the toroidal bubble at $z = 0.6$–$1.0D_{eq}$. The value of $V_e/V_{b,ref}$ decreases as the bubble continues to rise towards $z = h_{stable}$ (figure 10). Here, the travel distances $h_{stable}$ for the six $Fr$ cases correspond to $5.6$–$9.6D_{eq}$. Despite the long travel distance, the toroidal bubble can still transport approximately five times the volume of the lower liquid. Although the bubble and liquid conditions are not identical, our results suggest that toroidal bubbles have superior transport performance compared with bubbles of other shapes. Interestingly, while there are huge differences in $V_e/V_{b,ref}$ between the six $Fr$ cases at $z/h_{stable} < 0.5$, their values tend to collapse onto each other when $z/h_{stable} > 0.5$. Furthermore, the converged values of $V_e/V_{b,ref}$ at $z/h_{stable} = 1$ are in quite a narrow band between 4.3 and 6.0. This unique feature – convergence of the volume ratio $V_e/V_{b,ref}$ – is related to the balance of linear momentum of the ellipsoidal body, which is analysed in the following section.

### 3.3. *Prediction of temporal change in ring radius*

The relationship between the entrained volume and the ring radius, as shown in (3.1), indicates that the transport capability of a toroidal bubble can be evaluated from the temporal change in the ring radius of the bubble. In this section, we theoretically predict the temporal variation in the ring radius. The ring radius before passing the liquid–liquid interface is discussed first. When the bubble is far below the interface, the deformation of the interface is not observable; that is, the bubble has little effect on the interface. At this time, the behaviour of the toroidal bubble can be explained by referring to a toroidal bubble rising in a single liquid. For a single liquid, the theoretical ring radius $R$ is given by

$$R = \left[R_a^2 + \frac{F_B(t - t_a)}{\pi\rho_l \Gamma}\right]^{1/2}, \tag{3.2}$$

assuming that the circulation $\Gamma$ remains constant (Turner 1957). Here, $t_a$ is an arbitrary time, $R_a$ is the vortex ring radius at $t = t_a$ and $\rho_l$ is the density of the surrounding liquid. Additionally, $F_B$ is the buoyancy force acting on the toroidal bubble, which is assumed to remain constant: $F_B = (\rho_l - \rho_{air})gV_b$, where $\rho_{air} = 1.2\,\mathrm{kg\,m^{-3}}$. According to (3.2), the ring radius increases over time, which agrees with our observation at $t^* < 0$ in figure 6(*a*).

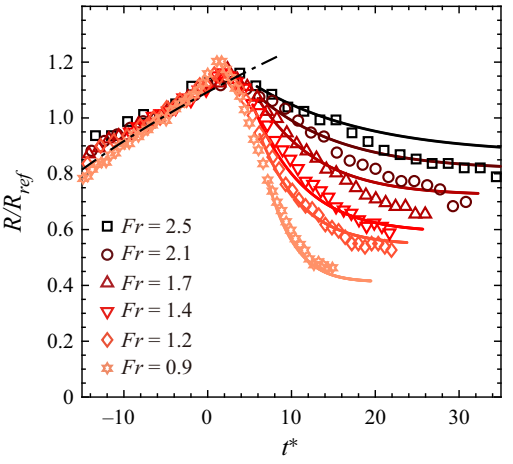


Figure 11. Comparison of normalised ring radius $R/R_{ref}$ between experimental measurements (markers) and numerical solutions of (3.10) (solid lines) for $Fr = 0.9$–$2.5$ ($\Lambda = 73.2$ and $At = 0.067$). The black dash–dotted line is from (3.5), and the solid lines are from (3.10).

Dividing both sides by $R_{ref}$ and substituting (2.3) gives the dimensionless form of (3.2):

$$\frac{R}{R_{ref}} = \left[1 + \frac{\rho_l - \rho_{air}}{\rho_l}\frac{gV_{b,ref}}{\pi\Gamma_{ref}^2}(t^* - t^*_{ref})\right]^{1/2} = \left[1 + \frac{1}{Fr^2}\frac{\rho_l - \rho_{air}}{\rho_l}\frac{V_{b,ref}}{\pi R_{ref}^3}(t^* - t^*_{ref})\right]^{1/2}, \tag{3.3}$$

where $t^*_{ref}$ is the dimensionless time at $t = t_{ref}$. Here, $t_a$, $R_a$, $\Gamma$ and $V_b$ are replaced by $t_{ref}$, $R_{ref}$, $\Gamma_{ref}$ and $V_{b,ref}$, respectively.

In figure 6($a$), $R/R_{ref}$ is hardly affected by $Fr$ before crossing the interface. The independence of $R/R_{ref}$ by $Fr$ can be derived as follows. Walters & Davidson (1963) theoretically estimated the circulation of the toroidal bubble, $\Gamma$, as

$$\Gamma = 3g^{1/2}V_b^{1/2}, \tag{3.4}$$

and showed that their experimental data were in reasonable agreement with (3.4) although this relation was derived from the instant when a spherical bubble deforms significantly and turns toroidal. In (3.3), the air density is negligible compared to the liquid density, and $V_b = V_{b,ref}$. Combining (3.4) with (3.3) yields

$$\frac{R}{R_{ref}} = \left[1 + \frac{1}{9\pi}(t^* - t^*_{ref})\right]^{1/2}, \tag{3.5}$$

which is independent of $Fr$. The dash–dotted line in figure 11 is from (3.5), which shows the theoretical prediction of the ring radius is in good agreement with the experimental data.

However, after passing the interface, the buoyancy force of the toroidal bubble is not the only force critical for the bubble dynamics. To take other forces into account without considering the complexity outside the ellipsoidal body, the boundary of the ellipsoidal body (figure 4$a$) is selected as a control surface. By doing so, mass flux across the control

surface appears only through the liquid column below the ellipsoidal body. As the control volume moves upwards at a propagation speed $U$, the $z$-momentum equation from the Reynolds transport theorem is given as

$$\sum F_z - \int_{CV} a_z \,\mathrm{d}m = \frac{\mathrm{d}}{\mathrm{d}t}\int_{CV} u_{z,rel}\,\mathrm{d}m + \int_{CS} u_{z,rel}\,\mathrm{d}\dot{m}_{out}, \tag{3.6}$$

where $a_z(=\mathrm{d}U/\mathrm{d}t)$ is the $z$-directional acceleration of the control volume with respect to the ground reference frame, and $u_{z,rel}$ is the $z$-directional velocity of flow relative to the reference frame moving with the control volume (White 2015). $CV$ and $CS$ represent the control volume and control surface, respectively. Here, $\mathrm{d}m$ is the differential mass of the fluid inside the control volume and $\mathrm{d}\dot{m}_{out}$ is the differential mass flow rate out of the control surface. The first and second terms on the left-hand side are the sum of the forces applied on the ellipsoidal body and the inertial force accounting for the accelerating control volume, respectively, and the first and second terms on the right-hand side are the momentum change within the control volume and the momentum flux through the control surface, respectively.

Some assumptions should be made because the exact velocity field inside the control volume cannot be obtained. We assume that the first term on the right-hand side of (3.6) is minor because the flow is circulatory around the ring core of the toroidal bubble and thus $u_{z,rel}$ inside the control volume is mostly cancelled out for volume integral. Although the downward flow near the lower region of the ellipsoidal body exists towards the liquid column, the temporal variation of the downward flow velocity is minimal. Because the momentum flux through the control surface occurs only through the liquid column descending from the ellipsoidal body, the second term on the right-hand side can be rewritten as $(\dot{m}u_{z,rel})_{out}$, where $\dot{m}$ at the outlet means the outward mass flow rate from the ellipsoidal body into the liquid column. As the momentum of the liquid column is relatively small compared with that of the ellipsoidal body, the liquid column is assumed to be nearly still in the ground reference frame, and the relative $z$-velocity $u_{z,rel}$ at the outlet is supposed to be equal to $-U$. That is, the second term on the right-hand side of (3.6) is dominant over the first term. Equation (3.6) is then simplified as

$$\sum F_z = m\frac{\mathrm{d}U}{\mathrm{d}t} - \dot{m}_{out}U = \frac{\mathrm{d}}{\mathrm{d}t}(mU), \tag{3.7}$$

where $\dot{m}_{out} = -\mathrm{d}m/\mathrm{d}t$; $m$ is the total mass inside the control volume.

For $z$-directional forces on the left-hand side in (3.7), the body force acting on the control volume and the surface force acting on the control surface should be considered. Neglecting air density, the gravitational body force acting on the ellipsoidal body in the downward direction is $\rho_l g V_e$, and the buoyancy force due to the hydrostatic pressure distribution on the surface of the ellipsoidal body is $\rho_u g(V_e + V_{b,ref})$ in the upward direction. To evaluate the drag from the pressure and shear stress distributed on the surface of the ellipsoidal body, we refer to Gan, Dawson & Nickels (2012) in which the drag force over the ellipsoidal boundary of the turbulent and single-phase vortex ring is obtained. The drag force acting on the ellipsoidal boundary in the downward direction is given by

$$F_D = C_D'' \times \frac{1}{2}\rho_u U^2 \times \pi R^2 k_4, \tag{3.8}$$

where $C_D''$ is the drag coefficient and $k_4$ is the geometrical coefficient related to the shape of the ellipsoidal body. According to their estimation, $C_D'' k_4$ is approximately 0.042 for their cases. The drag by the shear stress on the ellipsoidal boundary is an order of magnitude

smaller than the pressure drag for turbulent vortex rings. Because of similarity between the ellipsoidal boundary of the vortex ring noted by Gan *et al.* (2012) and the surface of the ellipsoidal body in our study, we adopt $C_D'' k_4 = 0.042$ and assume that the viscous drag is negligible; the effect of viscous drag is discussed again in § 3.4 with other experimental data using the three upper liquids with different viscosities.

The liquid column below the ellipsoidal body has an additional effect on the pressure for the lower surface of the ellipsoidal body (Ji, Yang & Feng 2021). The Laplace pressure due to the curvature of the liquid column, which acts on the lower surface, is $\sigma_I/R_c$, where $R_c$ is the curvature radius of the liquid column surface. Consequently, the force in the upward direction due to the Laplace pressure in the liquid column is approximately $(\sigma_I/R_c)\pi R_c^2$. Assuming that $R_c$ is of the same order of magnitude as $R$, this force can scale as $\pi\sigma_I R$, which is only 1/400 of the gravitational force acting on the ellipsoidal body. Therefore, the force by the Laplace pressure is negligible. In addition, the interfacial tension force acting on the region connecting the ellipsoidal body and the liquid column scales as $2\pi R\sigma_I$ and is negligible, considering that its scale is only approximately 1/200 of the gravitational force acting on the ellipsoidal body.

Substitution of the aforementioned forces into (3.7) leads to

$$(\rho_u - \rho_l) g V_e + \rho_u g V_{b,ref} - \frac{1}{2}\pi C_D'' k_4 \rho_u U^2 R^2 = \frac{\mathrm{d}}{\mathrm{d}t}(mU). \tag{3.9}$$

According to (3.1), $m(= \rho_l V_e)$ is a function of $R$; the mass of the toroidal bubble inside the ellipsoidal body is negligible. Also, from the assumption that the bubble volume remains constant, $V_b(= 2\pi^2 R a^2) = V_{b,ref}$ and $a = (V_{b,ref}/2\pi^2 R)^{1/2}$. Hence, (3.9) has two variables ($U$ and $R$), which can be reduced to one if we express $U$ in terms of $R$. If the passage through the interface does not significantly affect the circulation, $\Gamma$ can be replaced by $\Gamma_{ref}$, and $U$ can be expressed as a function of only $R$ in (2.1). Combining (2.1), (3.1) and (3.9) yields the equation for $R$,

$$\begin{aligned}
&(\rho_u - \rho_l) g (5.8R^3 + 0.6R_{ref}^3 - V_{b,ref}) + \rho_u g V_{b,ref} \\
&\quad - \frac{1}{2}\pi C_D'' k_4 \rho_u \left[ \frac{\Gamma_{ref}}{4\pi} \left\{ \frac{1}{2} \ln\left( \frac{128\pi^2 R^3}{V_{b,ref}} \right) - \frac{1}{4} \right\} \right]^2 \\
&= \frac{\mathrm{d}}{\mathrm{d}t} \left[ \rho_l (5.8R^3 + 0.6R_{ref}^3 - V_{b,ref}) \frac{\Gamma_{ref}}{4\pi R} \left\{ \frac{1}{2} \ln\left( \frac{128\pi^2 R^3}{V_{b,ref}} \right) - \frac{1}{4} \right\} \right].
\end{aligned} \tag{3.10}$$

Discretisation using the forward Euler method for $R$ with a time step of $\Delta t = 0.003$ s is employed to solve (3.10) numerically. Because (3.10) is derived under the condition in which the ellipsoidal body is fully formed after penetration, the numerical simulation uses the value of $R$ at $z = R_{ref}$, which is high enough to have the complete ellipsoidal body, as the initial condition.

Admittedly, the theoretical prediction from (3.10) has several limitations. As the ring radius decreases, the inward radial velocity makes the Kutta–Joukowski lift, accelerating the core upwards (Lundgren & Mansour 1991). Therefore, (2.1) that represents the relation between $U$ and $R$ needs to be modified after passing through the interface, especially for low $Fr$ where the bubble undergoes significant speed change. In addition, although we use a single drag coefficient $C_D''$ which was originally acquired for turbulent and single-phase vortex rings, the presence of the three phases in this study makes the detailed flow structure of the toroidal bubble differ from that of the turbulent vortex rings, which also causes errors in the theoretical prediction. Despite these limitations, the numerical

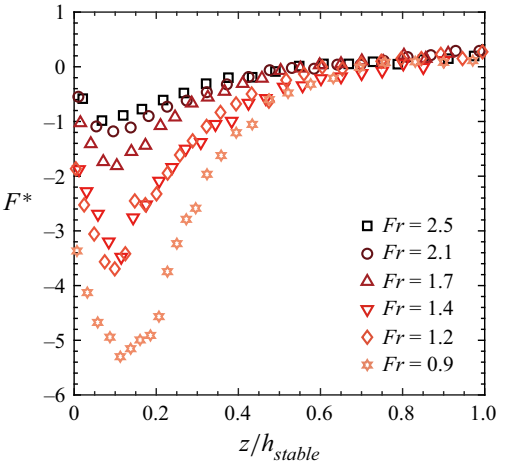


Figure 12. Normalised force in $z$-direction with respect to dimensionless height $z/h_{stable}$ of the toroidal bubble for $Fr = 0.9$–$2.5$ ($\Lambda = 73.2$ and $At = 0.067$).

solutions of (3.10) successfully capture the temporal change in the ring radius from the experiments (figure 11). This theoretical result explains that the downward force acting on the ellipsoidal body eventually leads to its contraction.

For a solid sphere passing through a horizontal liquid–liquid interface, Pierson & Magnaudet (2018) theoretically estimated the amount of liquid that adheres to the sphere and moves together, using vertical force balance acting on the sphere with buoyancy and surface tension forces. Even for a non-toroidal bubble coated with oil, the volume fraction of the bubble and oil is determined where the resultant force of vertical forces approaches zero (Ji *et al.* 2021). Similarly, we examine the vertical forces acting on the ellipsoidal body to find the relationship between the vertical forces and the entrained volume. Figure 12 plots the left-hand side of (3.10) (i.e. $\sum F_z$) with respect to the vertical position $z/h_{stable}$ of the bubble. Here, $\sum F_z$ is normalised by the buoyancy force acting on the bubble when it is immersed entirely in the lower liquid, $F_B$ in (3.2): $F^* = \sum F_z/F_B$. In figure 12, the vertical net force $F^*$ is very close to zero when the piercing of the upper liquid into the ellipsoidal body occurs at $z/h_{stable} = 1$ (figure 8). In other words, because $F^*$ close to zero causes slow change in the ring radius as inferred from (3.10), the liquid column becomes thinner, resulting in the piercing of the upper liquid.

As the piercing of the upper liquids occurs when the vertical forces acting on the ellipsoidal body balance each other, we can also predict the entrained volume at $z/h_{stable} = 1$ from the force balance in (3.9). From our observation, the magnitude of pressure drag is minimal at $z/h_{stable} = 1$ for all cases, while gravitational and buoyancy forces are dominant. Neglecting the pressure drag, the following approximation is valid at $z/h_{stable} = 1$:

$$(\rho_u - \rho_l)gV_{e,f} + \rho_u g V_{b,ref} \approx 0, \tag{3.11a}$$

$$\frac{V_{e,f}}{V_{b,ref}} \approx \frac{\rho_u}{\rho_l - \rho_u}, \tag{3.11b}$$

where $V_{e,f}$ is the entrained volume at $z/h_{stable} = 1$. For our cases, (3.11) yields $V_{e,f}/V_{b,ref} \approx 6.7$, which is very close to the experimental values of $V_e/V_{b,ref}$ at $z/h_{stable} = 1$ in figure 10. In short, the final value of the entrained volume is simply determined by the densities of the liquids and the bubble volume.

| $Fr$ | $\Lambda$ | $At$ | $R_{ref}$ (cm) | $U_{ref}$ (cm s$^{-1}$) | $V_{b,ref}$ (cm$^3$) | $\Gamma_{ref}$ (cm$^2$ s$^{-1}$) |
|---|---|---|---|---|---|---|
| 1.7 | 15.1 | 0.067 | 3.57 | 30.0 | 16.0 | 354.1 |
| 1.7 | 73.2 | 0.067 | 3.26 | 29.6 | 12.7 | 313.5 |
| 1.7 | 217.9 | 0.067 | 3.79 | 32.2 | 17.8 | 400.2 |

Table 3. Reference values of the toroidal bubbles in figures 13 and 14(*a–c*).

### 3.4. *Effects of viscosity and density difference*

Two dimensionless parameters, the viscosity ratio $\Lambda$ and the Atwood number $At$, are now controlled to explore how the dynamics of a toroidal bubble change with the relative magnitudes of viscosity and density between the two liquids. First, by changing the viscosity of the upper liquid, $\Lambda$ varies from 15.1 to 217.9, while $Fr$ and $At$ remain fixed at 1.7 and 0.067, respectively (three cases in table 3). Comparing the cases of $\Lambda = 15.1$ and 217.9, the overall sequential patterns of the toroidal bubble after crossing the interface are similar at the same $t^*$, although the interface of the liquid column is smoother for $\Lambda = 217.9$ (figure 13).

Obviously, the ring radius and propagation speed are not affected by the viscosity ratio before $t^* = 0$ because only the upper liquid has changed (figure 14*a*,*b*). After $t^* = 0$, however, the toroidal bubble exhibits faster radial contraction at given $t^*$ for higher $\Lambda$, leading to a slightly greater propagation speed. The solid lines in figure 14(*a*) are from the numerical solutions of (3.10). Note that (3.10) neglects the drag force from the viscous stress on the ellipsoidal body. Thus, it shows good accuracy in predicting the change in the ring radius for low $\Lambda$, but deviates from the experimental observations for high $\Lambda$. The viscous drag resists the upward motion of the ellipsoidal body, adding a downward force along with the gravitational force. As a result, a stronger viscous drag force would make the ellipsoidal body and bubble shrink more rapidly.

The entrained volume also exhibits a slightly faster decrease for the higher $\Lambda$, following the trend of $R/R_{ref}$ (figure 14*c*). As a consequence, $V_e/V_{b,ref}$ at $z = h_{stable}$ becomes smaller for the higher value of $\Lambda$. The values of $V_{e,f}/V_{b,ref}$ are 6.4 and 3.6 for $\Lambda$ = 15.1 and 217.9, respectively. Although not presented here, $V_e/V_{b,ref}$ tends to decrease with increasing $\Lambda$ for fixed values of $Fr$ other than 1.7 reported in figure 14(*c*). As discussed in § 3.3, the entrained volume is determined by the vertical forces imposed on the ellipsoidal body, and the entrained volume at $z = h_{stable}$ corresponds to a zero net vertical force in (3.11). However, the force acting on the surface of the ellipsoidal body from the viscous stress of the upper liquid was neglected in § 3.3 because of the difficulty in rigorously estimating the viscous stress. As a result, a stronger viscous drag force would make the ellipsoidal body and bubble shrink more rapidly, leading to the reduced $V_{e,f}/V_{b,ref}$ for higher $\Lambda$. The characteristic travel distance $h_{stable}/R_{ref}$ is almost unaffected by $\Lambda$ in the range considered in this study (figure 14*d*); for this plot, other cases with different $Fr$ values are included in addition to the three cases in table 3. This is because, for the higher $\Lambda$, the increase in the propagation speed owing to the faster reduction in the ring radius offsets the negative effect of the stronger viscous force on the travel distance.

Despite an increase in the viscosity ratio by a factor of approximately 15, the changes are relatively minor compared with those in figure 6, in which the effects of $Fr$ are depicted. In other words, changing the viscosity ratio has a limited effect on the interactions between the bubble and the interface compared with the Froude number, at least for the range of viscosities considered in this study. This is because the toroidal bubble does not directly

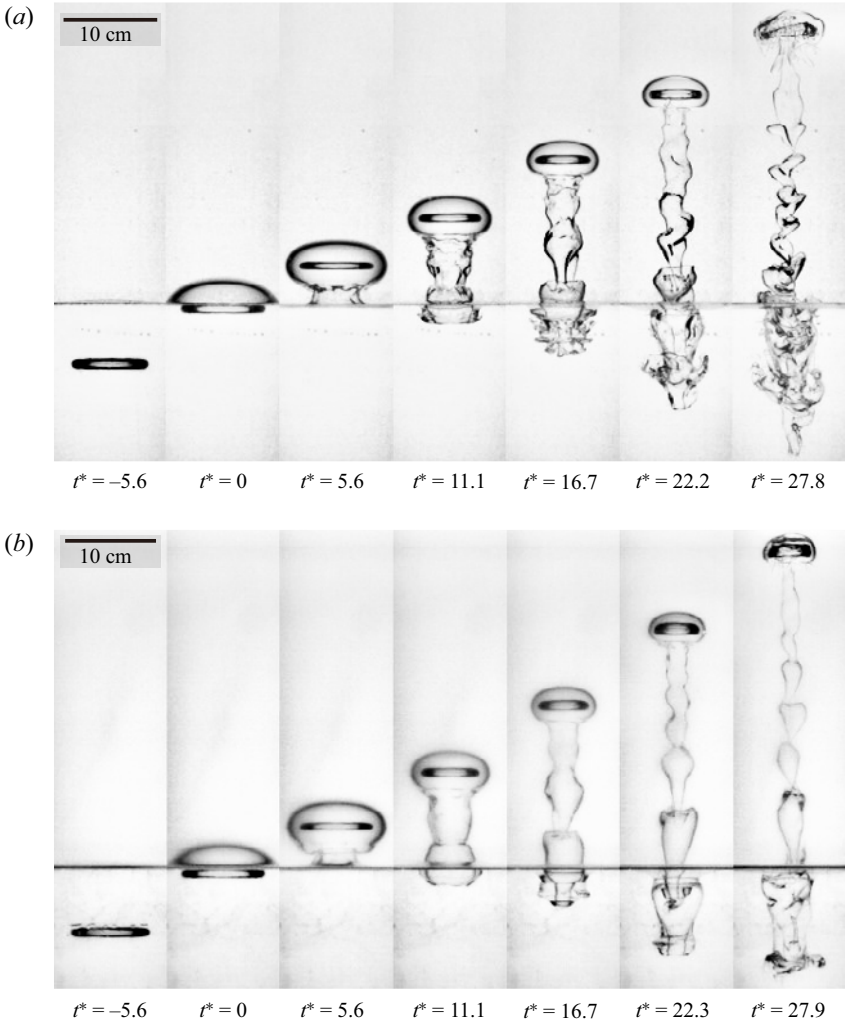


Figure 13. Sequential images of the toroidal bubble rising through an interface between two immiscible liquids for (*a*) $\Lambda = 15.1$ and (*b*) $\Lambda = 217.9$ ($Fr = 1.7$ and $At = 0.067$). See supplementary movie 3.

contact the upper liquid owing to the surrounding lower liquid. In contrast, non-toroidal bubbles penetrating through the interface are sensitive to the viscosity ratio since they undergo direct contact with the upper liquid (Greene *et al.* 1991; Bonhomme *et al.* 2012; Magnaudet & Mercier 2020; Choi & Park 2021).

Next, while the upper liquid (V2 oil) remains unchanged, the density of the lower liquid is varied using tap water and an NaCl solution to investigate the effect of the Atwood number between $At = 0.067$ and 0.133. The viscosity ratios of these two cases differ because the viscosity of the NaCl solution is greater than that of tap water: $\Lambda = 73.2$ for $At = 0.067$ and $\Lambda = 51.7$ for $At = 0.133$ (first two rows in table 4). Nevertheless, this difference is negligible because the bubble–interface interactions are insensitive to such small variations in the viscosity ratio, as explained previously.

For $At = 0.133$, the greater density of the lower liquid causes a stronger downward body force on the ellipsoidal body, resulting in a significant reduction in the ring radius at a given

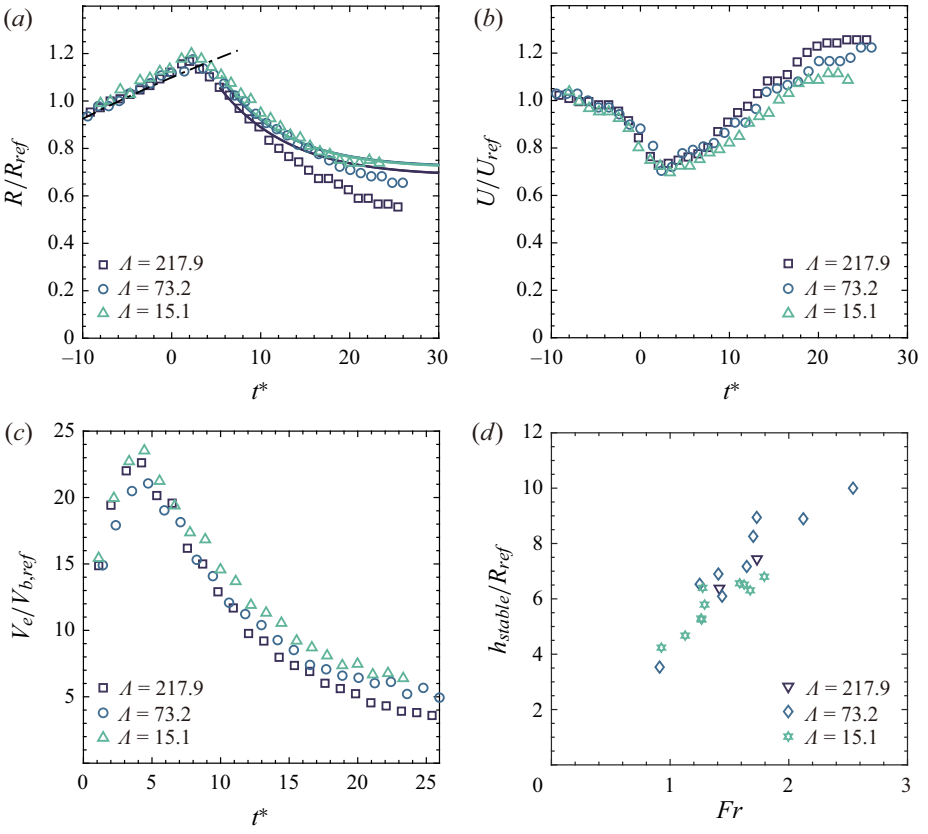


Figure 14. Temporal changes in (*a*) ring radius $R/R_{ref}$, (*b*) propagation speed $U/U_{ref}$ and (*c*) entrained volume $V_e/V_{b,ref}$ for $\Lambda = 15.1$, 73.2, 217.9 ($Fr = 1.7$ and $At = 0.067$). (*d*) Travel distance $h_{stable}/R_{ref}$ versus $Fr$ ($At = 0.067$). In panel (*a*), the black dash–dotted line is from (3.5), and the solid lines are from (3.10).

| $Fr$ | $\Lambda$ | $At$ | $R_{ref}$ (cm) | $U_{ref}$ (cm s$^{-1}$) | $V_{b,ref}$ (cm$^3$) | $\Gamma_{ref}$ (cm$^2$ s$^{-1}$) |
|---|---|---|---|---|---|---|
| 1.4 | 73.2 | 0.067 | 3.81 | 27.9 | 13.0 | 330.1 |
| 1.4 | 51.7 | 0.133 | 3.98 | 29.0 | 16.0 | 357.2 |
| 2.0 | 51.7 | 0.133 | 3.76 | 35.2 | 24.7 | 449.4 |

Table 4. Reference values of the toroidal bubbles. The first two rows are compared in figures 15 and 16(*a–c*), while the first and third are in figure 17(*a*,*b*).

time (figures 15 and 16*a*). Because of the greater mass in the ellipsoidal body for $At = 0.133$, the upward motion is more severely retarded immediately after the bubble crosses the interface (figure 16*b*). However, the greater contraction in the ring radius eventually induces a steeper increase in the propagation speed after $t^* = 6$. Remarkably, just a twofold increase in $At$ induces dramatic variations in $R/R_{ref}$ and $U/U_{ref}$, while their variations are minor despite a 15 times increase in $\Lambda$, as shown in figure 14(*a*,*b*). Also, in figure 16(*a*), the numerical solutions of (3.10) (solid lines) are in excellent agreement with the experimental results for both cases.

The higher Atwood number leads to a faster reduction in the entrained volume due to a significant contraction in the ring radius (figure 16*c*). Consequently, $V_e/V_{b,ref}$ at $z = h_{stable}$

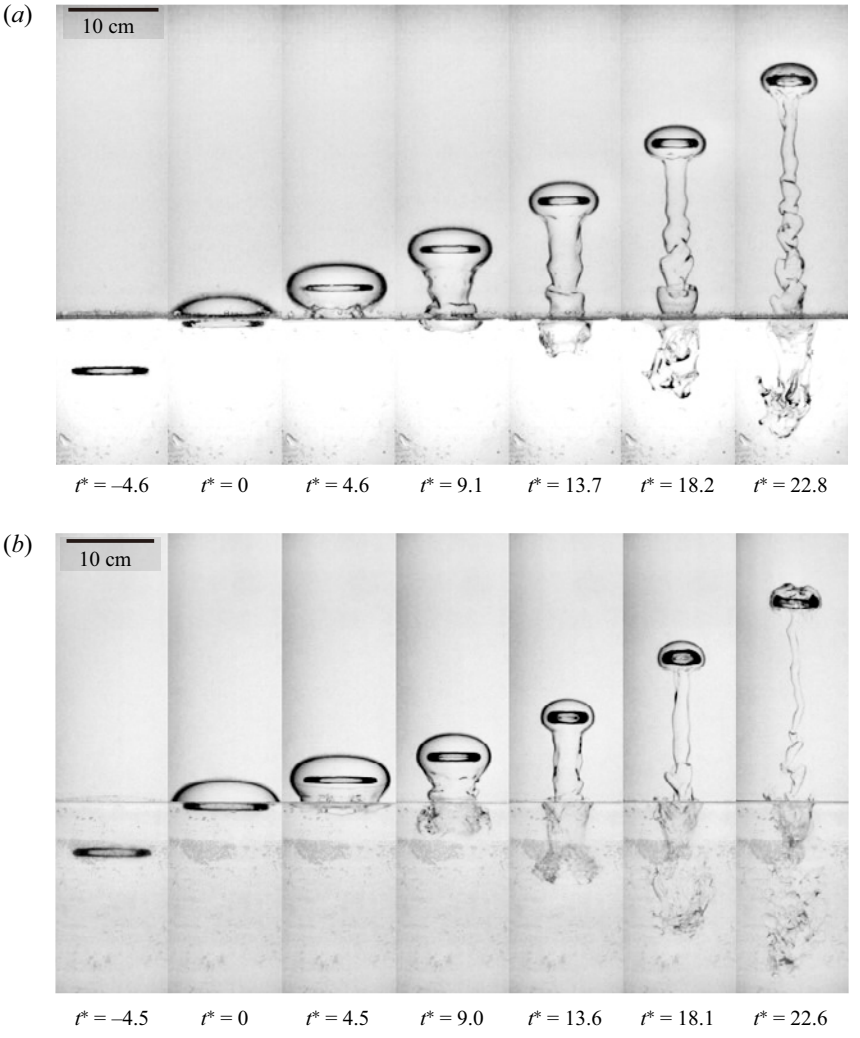


Figure 15. Sequential images of the toroidal bubble rising through an interface between two immiscible liquids for (*a*) $At = 0.067$, $\Lambda = 73.2$ and (*b*) $At = 0.133$, $\Lambda = 51.7$ ($Fr = 1.4$). See supplementary movie 4.

becomes smaller for the higher $At$: these values in figure 16(*c*) are 6.0 and 3.0 for $At$ = 0.067 and 0.133, respectively. Substituting the densities of the liquids used for $At = 0.133$ into (3.11) yields $V_{e,f}/V_{b,ref} \approx 3.2$, which matches well with the experimental value of $V_{e,f}/V_{b,ref} = 3.0$. Moreover, under a similar $Fr$ value, the travel distance $h_{stable}/R_{ref}$ is noticeably smaller for the higher $At$ because of the heavier lower liquid (figure 16*d*); additional cases with $Fr$ values other than 1.4 are considered for this plot. The value of $h_{stable}/R_{ref}$ is determined by $At$ rather than $\Lambda$, as seen from a comparison between figures 14(*d*) and 16(*d*).

In short, both the radius change and travel distance are more sensitive to $Fr$ and $At$ rather than $\Lambda$, given the ranges of these dimensionless parameters. Furthermore, in figures 6 and 16, the increase in $At$ and decrease in $Fr$ have similar effects on the variations in $R$ and $U$, as well as $h_{stable}$. Thus, it appears reasonable to introduce a dimensionless parameter that integrates the opposite effects of $Fr$ and $At$. Dahm *et al.* (1989) reported

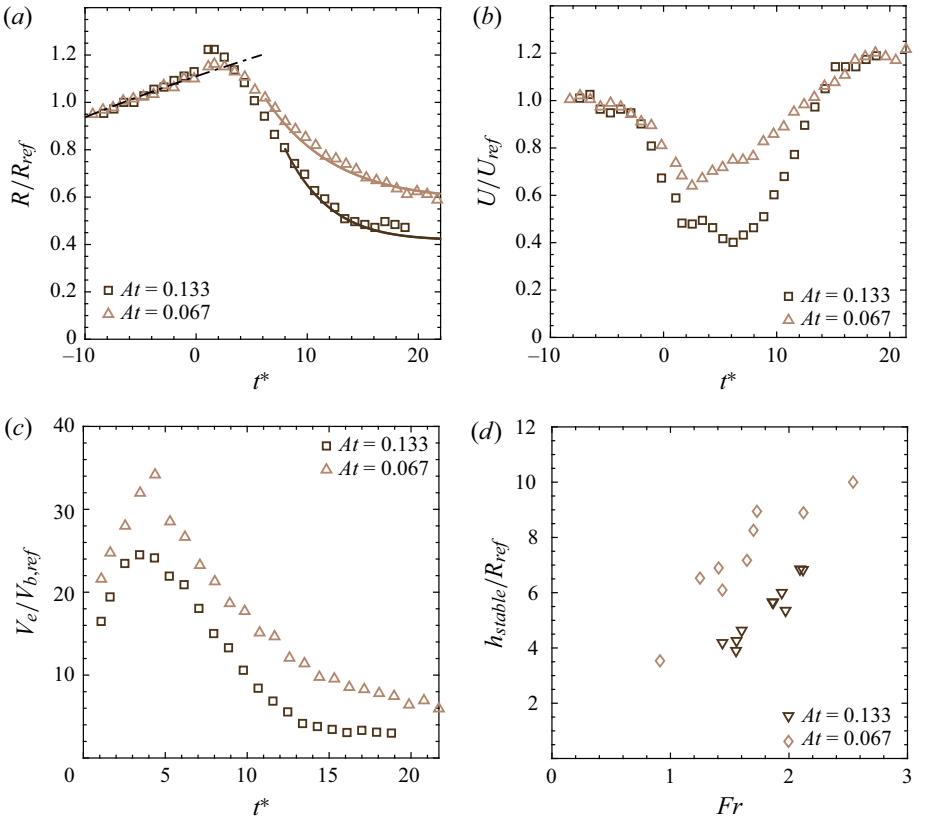


Figure 16. Temporal changes in (*a*) ring radius $R/R_{ref}$, (*b*) propagation speed $U/U_{ref}$ and (*c*) entrained volume $V_e/V_{b,ref}$ for $At = 0.067$ and 0.133 ($Fr = 1.4$). (*d*) Travel distance $h_{stable}/R_{ref}$ versus $Fr$. Here, $\Lambda = 73.2$ for $At = 0.067$ and $\Lambda = 51.7$ for $At = 0.133$. In panel (*a*), the black dash–dotted line is from (3.5), and the solid lines are from (3.10).

that, for a single-phase vortex ring impinging a density-stratified interface with a small density variation, the dynamics were primarily determined by $Fr$ divided by the square root of $At$. In some aspects, the interaction between a toroidal bubble and an interface between two immiscible liquids is similar to that of the single-phase vortex ring and the density-stratified interface. Accordingly, it is worth examining whether the *effective* Froude number $Fr_{eff} (= FrAt^{-1/2})$ can better characterise the toroidal bubble interacting with the immiscible interface.

For two cases with very similar $Fr_{eff}$ values (5.4 and 5.5), but distinctly different $Fr$ and $At$ values, $R/R_{ref}$ and $U/U_{ref}$ collapse onto each other at a given $t^*$ (figure 17*a*,*b*); these two cases correspond to the first and third rows in table 4. Furthermore, $h_{stable}/R_{ref}$ is collectively in a linear relation with $Fr_{eff}$ in figure 17(*c*). The feasible range of $Fr$ is limited in our apparatus, and there were not enough experimental cases to make identical $Fr_{eff}$ pairs, except for the cases of $Fr_{eff} \approx 5.5$ presented in figure 17. Due to experimental difficulties, we are able to validate only a few cases, so additional validation with wider ranges of $Fr$ and $At$ is essential to support the reliability of our argument. Nevertheless, the results in figure 17 indicate that the combined parameter $Fr_{eff}$ successfully reflects the effects of density difference between the two liquids.

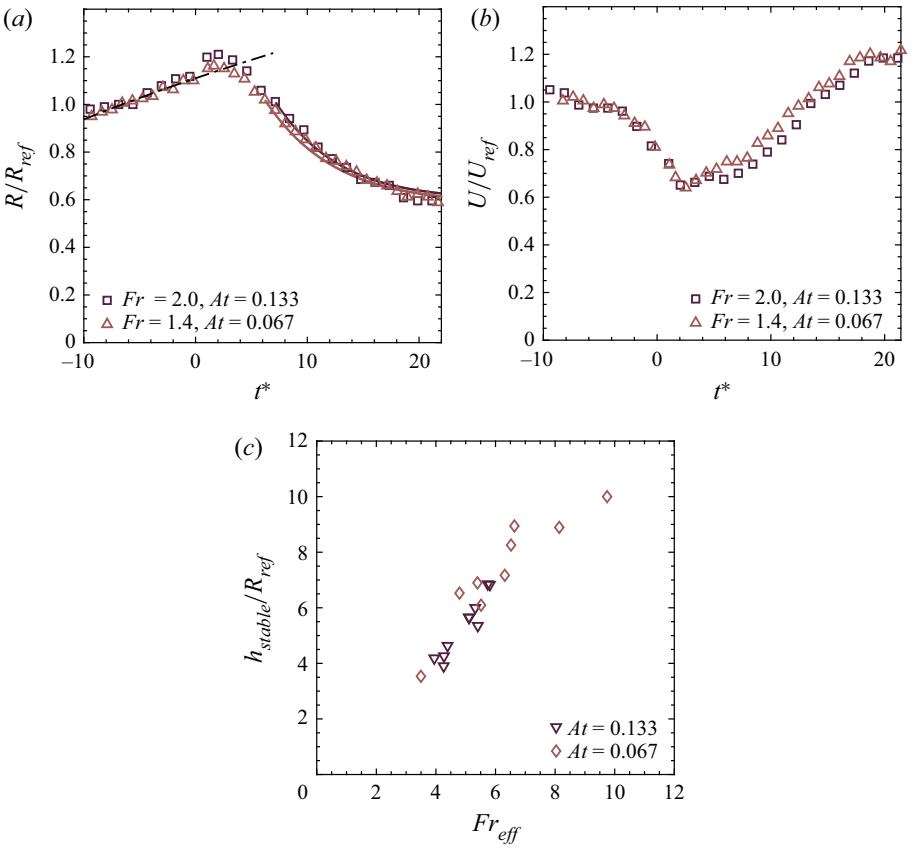


Figure 17. Temporal changes in (*a*) ring radius $R/R_{ref}$ and (*b*) propagation speed $U/U_{ref}$ for $Fr_{eff} = 5.4$ ($Fr = 2.0, At = 0.133$) and $Fr_{eff} = 5.5$ ($Fr = 1.4, At = 0.067$). (*c*) Travel distance $h_{stable}/R_{ref}$ versus $Fr_{eff}$ for the two $At$ values. In panel (*a*), the black dash–dotted line is from (3.5), and the solid lines are from (3.10).

Finally, using the effective Froude number, we briefly compare the penetration capability of a toroidal bubble with that of the single-phase vortex rings analysed in previous studies. The single-phase vortex ring can only partially penetrate the density-stratified interface and bounces backwards at $Fr_{eff} = 8.6$ in figure 7 of Dahm *et al.* (1989), and it does not penetrate the interface at $Fr_{eff} = 5.2$ in figure 7 of Stock *et al.* (2008). Furthermore, the single-phase vortex ring deforms the interface between immiscible liquids and rebounds without complete penetration even at $Fr_{eff} = 9.6$ in figure 7 of Song *et al.* (2021). By contrast, in the present study, the toroidal bubble clearly penetrates the interface at the small values of $Fr_{eff} = 3.5$ (figure 3*a*: $Fr = 0.9, At = 0.067$) and $Fr_{eff} = 3.9$ (figure 15*b*: $Fr = 1.4, At = 0.133$). Despite much smaller values of $Fr_{eff}$, the toroidal bubble can pass through the interface stably by virtue of the buoyancy force acting on the bubble, which implies that a toroidal bubble is capable of mixing surrounding liquids more easily across a broader range of conditions, compared with a single-phase vortex ring.

## 4. Concluding remarks

The vertical penetration of a rising toroidal bubble through a horizontal interface between two immiscible liquids has been investigated, with a particular focus on the transport of the lower liquid along with the toroidal bubble. When the toroidal bubble is far below

the horizontal interface, it slowly expands radially as it is immersed in a single liquid. However, significant changes in the bubble dynamics occur as it passes through the interface along with the considerable amount of surrounding heavier liquid in the form of an ellipsoid. Because of the downward gravitational force acting on the ellipsoidal body, the ring radius and propagation speed of the bubble decrease dramatically immediately after the bubble crosses the initial position of the interface. Although the volume of the entrained lower liquid diminishes as the bubble continues to rise, the bubble maintains a stable state until the upper liquid pierces into the enveloping lower liquid. At the instant of this piercing, the volume ratio of the entrained lower liquid and the bubble converges to a specific value. This convergence is caused by the balance of the buoyancy and gravitational forces exerted on the ellipsoidal body. Moreover, smaller $Fr$ and larger $At$ tend to reduce the ring radius, propagation speed and entrained volume at a given time after the bubble penetration, and decrease the travel distance up to the position where the bubble becomes unstable, while these quantities are relatively insensitive to $\Lambda$. The effective Froude number $Fr_{eff}(= FrAt^{-1/2})$ is employed to take into account the inertial and buoyancy effects together, and for similar $Fr_{eff}$, toroidal bubbles show almost identical behaviours.

The rising toroidal bubble has been found to carry a larger amount of the lower liquid to a higher position in the upper liquid by virtue of the surrounding vortical flow and superior flow entrainment performance. This remarkable feature of the toroidal bubble is advantageous in enhancing liquid transport and enlarging the interfacial area between two liquids. Although some representative characteristics of the bubble–interface interactions have been revealed in this fundamental study by varying the main dimensionless parameters, the comprehensive investigation of the entire lifecycle of the toroidal bubble is far from complete, particularly after the bubble becomes unstable. Furthermore, the mixing and transport behaviours should be robustly evaluated and optimised for practical application to fluid systems under various configurations of single or multiple toroidal bubbles.

**Supplementary movies.** Supplementary movies are available at https://doi.org/10.1017/jfm.2023.457.

**Funding.** This research was supported by the Basic Science Research Program through the National Research Foundation of Korea (NRF) funded by the Ministry of Science and ICT (NRF-2020R1A2C2102232) and by the Human Resources Program in Energy Technology of the Korea Institute of Energy Technology Evaluation and Planning (KETEP) granted financial resource from the Ministry of Trade, Industry & Energy, Republic of Korea (No. 20204030200050).

**Declaration of interests.** The authors report no conflict of interest.

**Author ORCIDs.**
Eunseong Moon https://orcid.org/0009-0005-7644-4534;
Minho Song https://orcid.org/0000-0002-8538-9769;
Daegyoum Kim https://orcid.org/0000-0002-7492-4631.

## Appendix A. Refraction correction

Light refracts on interfaces as the refractive indices of the liquids used in this study differ. Figure 18(*a*) shows the refraction of light associated with the vertical position of the bubble after it crosses the initial position of the interface. The camera is located at a distance $L$ from the wall of the glass tank and in line with the interface. The toroidal bubble rises vertically, maintaining a horizontal distance $L_1$ between the bubble centre and the wall. The thickness of the glass is neglected because it is small compared to $L$

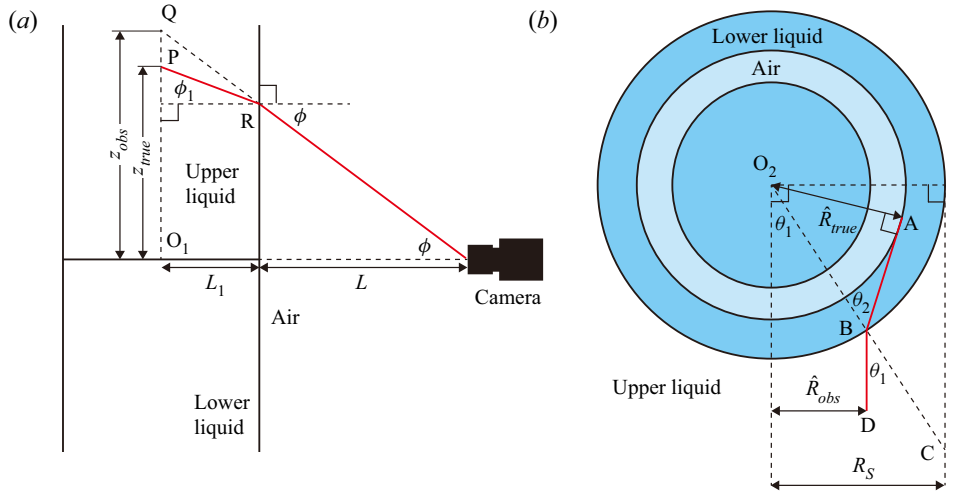


Figure 18. Refraction of light across (*a*) the wall of the glass tank and (*b*) the interface between the ellipsoidal body and the upper liquid. The red solid line denotes the path of light.

and $L_1$. Point P in figure 18 is an arbitrary point along the path of the bubble centre. Since the light from point P to the camera is deflected on the wall through point R (red solid line in figure 18*a*), the observed position in image is point Q with the corresponding observed vertical height $z_{obs}$. For the angle of incidence, $\phi_1$, and the angle of refraction, $\phi$, three equations are established: $z_{obs} = (L + L_1)\tan\phi$, $z_{true} = L\tan\phi + L_1\tan\phi_1$ and $\sin\phi/\sin\phi_1 = n_1$, where $n_1$ is the refractive index of the upper liquid (table 1). The distance between points $O_1$ and P is obtained by combining these equations, which yields

$$z_{true} = L\tan\phi + L_1\tan\left[\sin^{-1}\left(\frac{1}{n_1}\sin\phi\right)\right], \tag{A1}$$

where we set $L_1 = 22.5$ cm and $L = 240$ cm. Before the bubble passes the interface, the correction of the vertical position is also performed using the same method.

After penetration, the actual value of the ring radius inside the ellipsoidal body is different from the ring radius observed in the image. Thus, we correct the actual value of the ring radius with the assumption that the bubble and the ellipsoidal body are axisymmetric. The outer radius of the toroidal bubble, which is equal to the sum of the ring radius and core radius, is defined as $\hat{R}$: $\hat{R} = R + a$; see figure 2(*a*).

In figure 18(*b*) which depicts light refraction across the surface of the ellipsoidal body, the angle of incidence $O_2BA$ of the light travelling from point A on the interface of the bubble to point B on the surface of the ellipsoidal body is defined as $\theta_2$, and the angle of refraction CBD is defined as $\theta_1$. The length of the major axis of the ellipsoidal body, $R_s$, is equal to that of line segment $O_2B$. The actual value of $\hat{R}$, which is equal to the length of line segment $O_2A$, is $\hat{R}_{true} = R_s\sin\theta_2$. The observed value of $\hat{R}$ is $\hat{R}_{obs} = R_s\sin\theta_1$. From Snell's law, $\sin\theta_1/\sin\theta_2 = n_2/n_1$, where $n_2$ is the refractive index of the lower liquid (table 1). Combining the given equations, $\hat{R}_{true}$ is $(n_1/n_2)\hat{R}_{obs}$.

With $\hat{R}_{true}$ known, we can then estimate the actual ring radius $R_{true}$. Assuming that the bubble is axisymmetric with a perfectly circular core and its volume remains constant along the propagation, the bubble volume should be $V_{b,ref} = 2\pi^2 R_{true}a_{true}^2$. From $a_{true} = \hat{R}_{true} - R_{true}$, $V_{b,ref} = 2\pi^2 R_{true}(\hat{R}_{true} - R_{true})^2$. Because the $V_{b,ref}$ value on the left-hand

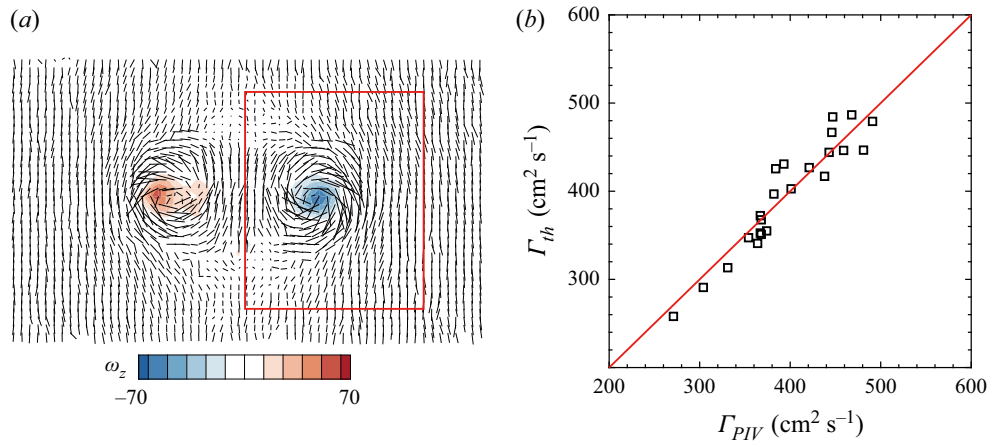


Figure 19. (*a*) Closed curve to compute circulation $\Gamma$. (*b*) Circulation around the toroidal bubble from (2.1), $\Gamma_{th}$, with respect to that obtained from PIV, $\Gamma_{PIV}$. The red solid line denotes $\Gamma_{th} = \Gamma_{PIV}$.

side of this relationship is acquired from the phase before penetration, $R_{true}$ can be obtained by solving the cubic equation and selecting a reasonable one among the three solutions.

## Appendix B. Experimental measurement of vortex circulation

The velocity fields around a toroidal bubble were acquired in water by using PIV to obtain circulation around the bubble. For the measurement of circulation, experiments were performed only in water without the upper liquid, and other conditions are the same as those given in § 2. The circulation is defined as

$$\Gamma = \int_C u_t \, \mathrm{d}l = \sum_C u_t \Delta l, \tag{B1}$$

where $C$ is a closed curve, $u_t$ is the tangential velocity component along $C$, $\Delta l$ is the differential line segment of $C$ and $\Delta l$ is the spatial resolution of the velocity fields from PIV. Here, the closed curve $C$ was set to be sufficiently large to include the area with non-zero vorticity around the toroidal bubble; see figure 19(*a*). The circulation was calculated when the toroidal bubble was positioned 60 cm above the hole of the bubble generator, which is similar to the reference position. The circulation obtained from PIV, $\Gamma_{PIV}$, was compared with that predicted by (2.1), $\Gamma_{th}$, for 23 cases in the range of $\Gamma_{PIV} = 271$–$491\ \mathrm{cm^2\ s^{-1}}$ (figure 19*b*). The mean of the relative error, defined as $(\Gamma_{PIV} - \Gamma_{th})/\Gamma_{PIV}$, for these 23 cases was 0.38 %, with a mean absolute percentage error of 4.28 % and an R-squared value of 0.86.

## References

Advaith, S., Manu, K.V., Tinaikar, A., Chetia, U.K. & Basu, S. 2017 Interaction of vortex ring with a stratified finite thickness interface. *Phys. Fluids* **29**, 093602.

Bonhomme, R., Magnaudet, J., Duval, F. & Piar, B. 2012 Inertial dynamics of air bubbles crossing a horizontal fluid–fluid interface. *J. Fluid Mech.* **707**, 405–443.

Bonometti, T. & Magnaudet, J. 2006 Transition from spherical cap to toroidal bubbles. *Phys. Fluids* **18**, 052102.

Cao, Y. & Macián-Juan, R. 2020 Numerical investigation of central breakup of large bubble induced by liquid jet. *Phys. Fluids* **32**, 033302.

CHANG, C. & LLEWELLYN SMITH, S.G. 2018 The motion of a buoyant vortex filament. *J. Fluid Mech.* **857**, R1.

CHEN, L., GARIMELLA, S.V., REIZES, J.A. & LEONARDI, E. 1999 The development of a bubble rising in a viscous liquid. *J. Fluid Mech.* **387**, 61–96.

CHENG, M., LOU, J. & LIM, T.T. 2013 Motion of a bubble ring in a viscous fluid. *Phys. Fluids* **25**, 067104.

CHOI, K. & PARK, H. 2021 Interfacial phenomena of the interaction between a liquid–liquid interface and rising bubble. *Exp. Fluids* **62**, 126.

DABIRI, J.O. & GHARIB, M. 2004 Fluid entrainment by isolated vortex rings. *J. Fluid Mech.* **511**, 311–331.

DAHM, W.J.A., SCHEIL, C.M. & TRYGGVASON, G. 1989 Dynamics of vortex interaction with a density interface. *J. Fluid Mech.* **205**, 1–43.

DIETRICH, N., PONCIN, S., PHEULPIN, S. & LI, H.Z. 2008 Passage of a bubble through a liquid–liquid interface. *AIChE J.* **54**, 594–600.

EMERY, T.S., RAGHUPATHI, P.A. & KANDLIKAR, S.G. 2018 Flow regimes and transition criteria during passage of bubbles through a liquid–liquid interface. *Langmuir* **34**, 6766–6776.

GAN, L., DAWSON, J.R. & NICKELS, T.B. 2012 On the drag of turbulent vortex rings. *J. Fluid Mech.* **709**, 85–105.

DE GENNES, P.-G., BROCHARD-WYART, F. & QUÉRÉ, D. 2004 *Capillarity and Wetting Phenomena: Drops, Bubbles, Pearls, Waves*. Springer.

GHORBANPOUR-ARANI, A., RAHIMIAN, M.-H. & HAGHANI-HASSAN-ABADI, R. 2020 Numerical simulation of dissolved air flotation using a lattice Boltzmann method. *Phys. Rev.* E **101**, 023105.

GREENE, G.A., CHEN, J.C. & CONLIN, M.T. 1991 Bubble induced entrainment between stratified liquid layers. *Intl J. Heat Mass Transfer* **34**, 149–157.

JI, B., YANG, Z. & FENG, J. 2021 Oil-coated bubble formation from submerged coaxial orifices. *Phys. Rev. Fluids* **6**, 033602.

LESAGE, P., KEMIHA, M., PONCIN, S., MIDOUX, N. & LI, H.Z. 2016 Mimicking dolphins to produce ring bubbles in water. *Biomimetics* **1**, 6.

LINDEN, P.F. 1973 The interaction of a vortex ring with a sharp density interface: a model for turbulent entrainment. *J. Fluid Mech.* **60**, 467–480.

LUNDGREN, T.S. & MANSOUR, N.N. 1991 Vortex ring bubbles. *J. Fluid Mech.* **224**, 177–196.

MAGNAUDET, J. & MERCIER, M.J. 2020 Particles, drops, and bubbles moving across sharp interfaces and stratified layers. *Annu. Rev. Fluid Mech.* **52**, 61–91.

MAGNAUDET, J. & MOUGIN, G. 2007 Wake instability of a fixed spheroidal bubble. *J. Fluid Mech.* **572**, 311–337.

MAO, N., KANG, C., TENG, S. & MULBAH, C. 2020 Formation and detachment of the enclosing water film as a bubble passes through the water–oil interface. *Colloids Surf.* A **586**, 124236.

MAXWORTHY, T. 1972 The structure and stability of vortex rings. *J. Fluid Mech.* **51**, 15–32.

MAZUMDAR, D. & GUTHRIE, R.I.L. 1995 The physical and mathematical modelling of gas stirred ladle systems. *ISIJ Intl* **35**, 1–20.

MCKIM, B., JEEVANJEE, N. & LECOANET, D. 2020 Buoyancy-driven entrainment in dry thermals. *Q. J. R. Meteorol. Soc.* **146**, 415–425.

NATSUI, S., NASHIMOTO, R., NAKAJIMA, D., KIKUCHI, T. & SUZUKI, R.O. 2018 Column and film lifetimes in bubble-induced two-liquid flow. *Phys. Rev.* E **97**, 062802.

NORBURY, J. 1973 A family of steady vortex rings. *J. Fluid Mech.* **57**, 417–431.

OLSTHOORN, J. & DALZIEL, S.B. 2017 Three-dimensional visualization of the interaction of a vortex ring with a stratified interface. *J. Fluid Mech.* **820**, 549–579.

PEDLEY, T.J. 1968 The toroidal bubble. *J. Fluid Mech.* **32**, 97–112.

PIERSON, J.-L. & MAGNAUDET, J. 2018 Inertial settling of a sphere through an interface. Part 1. From sphere flotation to wake fragmentation. *J. Fluid Mech.* **835**, 762–807.

REITER, G. & SCHWERDTFEGER, K. 1992 Observations of physical phenomena occurring during passage of bubbles through liquid/liquid interfaces. *ISIJ Intl* **32**, 50–56.

SHARAF, D.M., PREMLATA, A.R., TRIPATHI, M.K., KARRI, B. & SAHU, K.C. 2017 Shapes and paths of an air bubble rising in quiescent liquids. *Phys. Fluids* **29**, 122104.

SINGH, K.K., GEBAUER, F. & BART, H.-J. 2017 Bouncing of a bubble at a liquid–liquid interface. *AIChE J.* **63**, 3150–3157.

SONG, M., BERNAL, L.P. & TRYGGVASON, G. 1992 Head-collision of a large vortex ring with a free surface. *Phys. Fluids* A **4**, 1457–1466.

SONG, M., CHOI, S. & KIM, D. 2021 Interactions of the interface of immiscible liquids with an impinging vortex ring. *Phys. Fluids* **33**, 022108.

STOCK, M.J., DAHM, W.J.A. & TRYGGVASON, G. 2008 Impact of a vortex ring on a density interface using a regularized inviscid vortex sheet method. *J. Comput. Phys.* **227**, 9021–9043.

TRIPATHI, M.K., SAHU, K.C. & GOVINDARAJAN, R. 2015 Dynamics of an initially spherical bubble rising in quiescent liquid. *Nat. Commun.* **6**, 6268.

TURNER, J.S. 1957 Buoyant vortex rings. *Proc. R. Soc. Lond.* A **239**, 61–75.

VASEL-BE-HAGH, A.R., CARRIVEAU, R. & TING, D.S.-K. 2015*a* A balloon bursting underwater. *J. Fluid Mech.* **769**, 522–540.

VASEL-BE-HAGH, A.R., CARRIVEAU, R., TING, D.S.-K. & TURNER, J.S. 2015*b* Drag of buoyant vortex rings. *Phys. Rev.* E **92**, 043024.

WALKER, J.D.A., SMITH, C.R., CERRA, A.W. & DOLIGALSKI, T.L. 1987 The impact of a vortex ring on a wall. *J. Fluid Mech.* **181**, 99–140.

WALTERS, J.K. & DAVIDSON, J.F. 1963 The initial motion of a gas bubble formed in an inviscid liquid. Part 2. The three-dimensional bubble and the toroidal bubble. *J. Fluid Mech.* **17**, 321–336.

WANG, L. & FENG, L.-H. 2022 Dynamics of the interaction of synthetic jet vortex rings with a stratified interface. *J. Fluid Mech.* **943**, A1.

WANG, Q.X., YEO, K.S., KHOO, B.C. & LAM, K.Y. 2005 Vortex ring modelling of toroidal bubbles. *Theor. Comput. Fluid Dyn.* **19**, 303–317.

WHITE, F.M. 2015 *Fluid Mechanics*. McGraw-Hill.

XU, Y., HE, G.S., KULKARNI, V. & WANG, J.J. 2017 Experimental investigation of influence of Reynolds number on synthetic jet vortex rings impinging onto a solid wall. *Exp. Fluids* **58**, 6.

YAN, X., CARRIVEAU, R. & TING, D.S.-K. 2018 Laminar to turbulent buoyant vortex ring regime in terms of Reynolds number, Bond number, and Weber number. *Trans. ASME J. Fluids Engng* **140**, 054502.

YEO, K.W.B., KOH, J.Y., LONG, J. & NEW, T.H. 2020 Flow transitions in collisions between vortex-rings and density interfaces. *J. Vis.* **23**, 783–791.